Journal of Materials Chemistry C

ROYAL SOCIETY OF CHEMISTRY

REVIEW

View Article Online
View Journal | View Issue

Cite this: J. Mater. Chem. C, 2025, 13, 20444

Emerging chiral molecular carbon materials for chiroptoelectronic applications

Xinyang Zhang,[a] Xinyang Ge,[a] Jingya You,[a] Yipu Wang,*[a] Qiang Huang *[a] and Li Wan *[b]

Chirality is a ubiquitous phenomenon in nature and continues to inspire modern materials science. Among various chiral systems, chiral carbon materials have been extensively developed, with their chirality flexibly tuned through molecular-level chemical design and further amplified by solid-state intermolecular assembly. By incorporating different functional groups, these carbon materials can be tailored to exhibit excellent light-emitting and light-absorbing properties, making their chiral forms suitable for emitting or detecting circularly polarized light. In this review, we first introduce the basic concepts of chiral materials and spectroscopic chiroptical responses, and explain how chirality is introduced into molecular carbon systems through chemical design. We then systematically summarize recent research progress in chiral optoelectronic (chiroptoelectronic) applications that incorporate chiral carbon materials. Furthermore, we analyze the dissymmetry factors of each system and offer perspectives on strategies to enhance performance. We believe that this review will attract broad attention from interdisciplinary researchers working on carbon materials, chirality science, and optoelectronics.

Received 2nd July 2025,
Accepted 11th September 2025

DOI: 10.1039/d5tc02532j

rsc.li/materials-c

1. Introduction

Chirality is a ubiquitous phenomenon pervasive in nature. For instance, naturally occurring amino acids predominantly exhibit an L-configuration, while the ribose components in nucleic acids (DNA/RNA) are exclusively D-configurations.[1,2] Chirality emerges when a material is not superimposable on its mirror image, resulting in distinct structural differences between the substance and its enantiomeric counterpart. At the molecular level, chirality refers to two molecules with identical composition but mirror-symmetric configurations or conformations that cannot be superimposed.[3] At larger scales, the chirality extends to asymmetrical intermolecular assemblies or frameworks.[4] This geometric feature is critical for enabling materials to emit circularly polarized light, a prerequisite for chiroptoeletronic applications.

[a] School of Chemistry and Chemical Engineering, Nantong University, Nantong, 226019, China. E-mail: wangyipu@ntu.edu.cn, huangqiang@ntu.edu.cn
[b] Max Planck Institute of Microstructure Physics, Halle, 06120, Germany. E-mail: li.wan@mpi-halle.mpg.de

Yipu Wang

Yipu Wang received his PhD from East China University of Science and Technology in 2022 and joined Prof. Ben Zhong Tang's group as a postdoctoral researcher. He is now a research associate at Nantong University, focusing on the synthesis and application development of efficient aggregation-induced emission materials and clusteroluminescence materials.

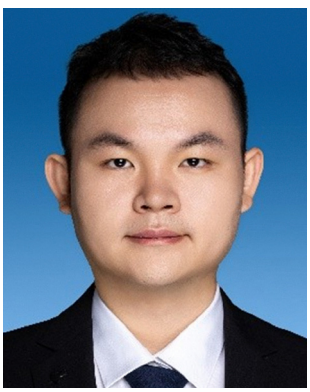

Qiang Huang

Qiang Huang is a Professor at Nantong University. He earned his PhD in Materials Science from the University of Science and Technology of China in 2020, followed by research positions at Technische Universität Dresden and the Max Planck Institute of Microstructure Physics. His research group focuses on the synthesis topological molecular carbons, targeting applications in optoelectronics, supramolecular systems, and advanced functional materials.

The ability of a material to emit circularly polarized light, or also known as circularly polarized luminescence (CPL), is related to the electronic structure of asymmetrically structured materials. This phenomenon manifests as differential emission of left-handed CPL and right-handed CPL (LH-CPL and RH-CPL).[5] To achieve CPL in molecular emitters, specific asymmetric arrangements of intramolecular chiral centers or three-dimensional stereochemical configurations are required. These should be merged or overlapped with chromophores in the molecular designs.[6]

Carbon materials are substances primarily composed of carbon atoms, which form diverse allotropes through unique bonding configurations. Key types of carbon materials include diamond, graphite, amorphous carbon and molecular-scale carbon structures.[7] In this review, we focus on molecular carbon materials, including helicenes,[8] chiral nanographenes,[9] chiral fullerenes,[10] and their derivatives. These chiral carbon materials are highly structurally tunable, enabling the construction of diverse chiral structures required for achieving CPL.[11] Their chiroptical and optoelectronic properties can be further tailored through molecular design strategies such as π-conjugation extension and heteroatom doping as well as by adopting inherently twisted or non-planar structures. Important optoelectronic parameters such as carrier mobility, luminescence efficiency, and emission behavior can be further optimized through chemical modification or film processing, which provides a promising route toward high-performance CPL-active materials. Based on the stereochemical origin of chirality, emissive chiral carbon materials can be classified into four major categories: point, axial, planar and helical chirality.[12] The point chirality originates from a tetrahedral atom (*e.g.*, sp^3 carbon) bonded to four distinct functional groups, while the axial chirality could originate from restricted rotation around a molecular axis (*e.g.*, biaryl systems), such as the atropisomers of 1,1′-bi-2-naphthol (BINOL).[13] In addition, asymmetric substitution on a molecular plane could lead to planar chirality, for example, through the asymmetric modification of the cyclopentadienyl rings in ferrocene derivatives. One of the most extensively studied types of molecular chirality is helical chirality, which originates from the twisted, screw-like geometry of certain molecules. This form of chirality is typically achieved by angularly fusing multiple aromatic rings, resulting in a rigid three-dimensional helical structure. Helicenes are a well-known example. In these molecules, the entire carbon backbone is intrinsically chiral due to its helical configuration.[14] Such diversity of chiral materials makes chirality control the core challenge in constructing functional materials. Chirality control strategies can be divided into two major paradigms in asymmetrical chemical reactions: stochastic approaches and deterministic approaches.[15,16] The former relies on statistical distributions or dynamic equilibria, while the latter guides the precise formation of chiral structures through predefined molecular design or external conditions. Kinetic and thermodynamic factors co-regulate this process: kinetic control governs product distribution *via* transition state energy barriers,[17] whereas thermodynamic control dominates equilibrium states through energy minimization.[18] Therefore, the precise realization of chirality control requires the integration of molecular design, environmental modulation, and dynamic process analysis. This provides critical guidance for the development of supramolecular functional materials, such as CPL materials.

Li Wan

Li Wan is a junior research group leader and an ERC starting grant awardee at the Max Planck Institute of Microstructure Physics in Germany. He started working on chiral materials since 2017, and received his PhD at Imperial College London (UK) in 2020. His research group investigates a wide range of chiral organic and hybrid semiconducting materials for circular polarization enhanced optoelectronic applications.

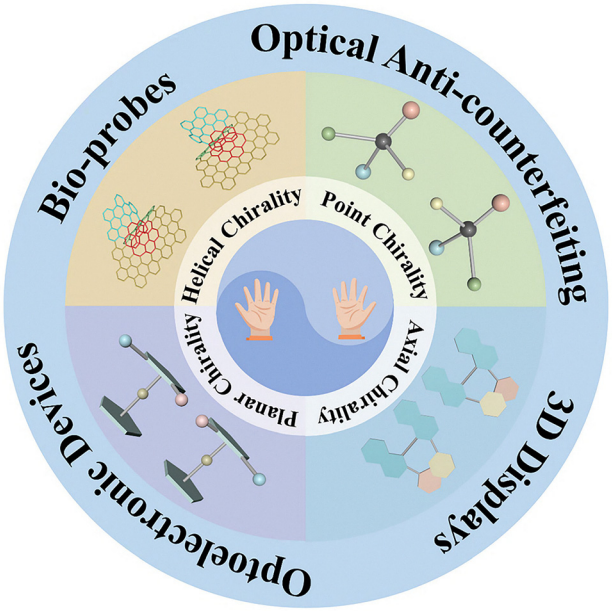

Fig. 1 Chirality classification and applications of molecular chiral carbons.

To date, chiral carbon-based systems have rapidly advanced through extensive scientific efforts, driven by the synergistic collaboration of chemical synthesis, spectroscopy, and device physics. These materials now show great promise as versatile platforms for CPL applications, enabling progress in fields such as next-generation 3D displays,[19] biological probes,[20] optoelectronic devices,[21] biological imaging,[22] and optical anti-counterfeiting techniques[23] (Fig. 1).

2. Key figures of merit in chiral molecular systems and their optoelectronic applications

For emissive chiral molecular systems, the chiroptical responses are routinely characterized by their chiral absorption properties,

i.e., circular dichroism (CD) with corresponding absorption dissymmetry factor (g_{abs}), and emission properties, *i.e.*, luminescent dissymmetry factor (g_{lum}). These parameters correspond to the chiral optical properties of the material in different states and exhibit a close correlation.[24]

CD reflects the differential absorption of LH- and RH-circularly polarized light by the material in its ground state. It is quantified by the difference in absorption coefficients ($\Delta\varepsilon$), typically measured *via* CD spectroscopy. $\Delta\varepsilon$ is defined as follows:

$$\Delta\varepsilon = \varepsilon_L - \varepsilon_R \quad (1)$$

where ε_L and ε_R are the molar absorption coefficients of LH- and RH-circularly polarized light.

The g_{abs}, a dimensionless metric derived from CD, is defined as follows:

$$g_{abs} = \frac{2(\varepsilon_L - \varepsilon_R)}{\varepsilon_L + \varepsilon_R} \quad (2)$$

where g_{abs} ranges from −2 to 2, with higher absolute values indicating stronger ground-state chirality.

In terms of chiral emission, g_{lum} characterizes the differential emission of LH- and RH-circularly polarized light in the excited state:

$$g_{lum} = \frac{2(I_L - I_R)}{I_L + I_R} \quad (3)$$

where I_L and I_R are the intensity of LH- and RH-circularly polarized light emitted from the material. It also ranges from −2 to 2, directly determining the CPL performance.

In bridging the chiral structures and potential device performance, CPL brightness (B_{CPL}) was introduced as a new tool recently to quantify the overall efficiency of circularly polarized emitters.[25] B_{CPL} is defined as follows:

$$B_{CPL} = \varepsilon \times \Phi_{PL} \times \frac{|g_{lum}|}{2} \quad (4)$$

where ε characterizes the material's capacity to absorb light at the excitation wavelength, and the luminescence quantum yield (Φ_{PL}) describes the efficiency of converting excited-state energy into photons, with a value between 0 and 1.

3. Chirality realization in molecular carbon materials

3.1 Point chirality

Point chirality, a fundamental form of molecular chirality, arises from the spatial asymmetric arrangement of groups around a chiral center. Point chiral luminophores, through synergistical integration of chiral centers with luminescent functionalities, exhibit exceptional tunability and diverse modulation capabilities. The key advantage lies in the controllable design of intramolecular chiral centers, racemization stability and precise modulation of luminescence properties. By modifying chiral centers, the spatial relative orientation of the electric transition dipole moment (μ_e) and magnetic transition dipole moment (μ_m) can be directionally controlled, thereby achieving luminescence properties with a high asymmetry factor ($|g| \propto \mu_e/\mu_m$)[26] and a narrow full width at half maximum (FWHM).[27]

In isolated point-chiral molecules, the $|g_{lum}|$ could be constrained by the spatial separation between the chiral center and luminescent moieties. For instance, a chiral cyclohexanediamine-based fluorophore developed by Zuo *et al.* in 2020 exhibited $|g_{lum}|$ values of only 10^{-4}–10^{-3} in toluene solution.[28] The performance limitations of point-chiral luminescent chromophores, which are usually caused by weak excitonic chiral coupling between the chromophores and their adjacent stereogenic centers,[29] have attracted significant research attention in recent years. In 2025, Wang *et al.* successfully developed novel high B_{CPL} point-chiral anthraquinone luminophores through a J-type supramolecular stacking approach (slip-stacked arrangement).[30] They designed two compounds—acetylene-linked **1** and linker-free **2** (Fig. 2a)—along with their respective precursor compounds (**3** and **4**, Fig. 2b). By incorporating amide groups into the point-chiral anthraquinone emitters, they established directional hydrogen bonds that facilitated efficient chirality transfer from peripheral stereocenters to the anthraquinone core. Structural planarization *via* alkynyl insertion ($\Delta\theta = 31.6^\circ$) correlates with a 15-fold CPL brightness enhancement (13.8 M^{-1} cm^{-1}), while FRET-mediated energy funneling permits on-demand color tuning.

3.2 Axial chirality

Axially chiral compounds exhibit optically active conformational isomers due to the presence of a rotationally restricted single bond within the molecule, which is referred to as the chiral axis. Taking thermally activated delayed fluorescence (TADF) materials as an example, traditional HOMO–LUMO separated TADF molecules feature distinct donor and acceptor moieties linked by a single bond that effectively disrupts conjugation while permitting significant geometric torsion. This configuration highly localizes the HOMO and LUMO on separate molecular units,[31] concurrently providing an ideal molecular framework for realizing axial chirality. Axial chirality, as an asymmetrical property at the molecular-level, has recently demonstrated unique application potential in luminescent materials, particularly excelling in TADF type organic light-emitting diodes (OLEDs).

In 2020, Chen *et al.* proposed a chiral emitting skeleton strategy (Fig. 3b) for designing axial TADF enantiomers, successfully synthesizing blue-emitting materials with high photoluminescence efficiency and circularly polarized electroluminescence (CPEL) performance.[32] By coupling two non-chiral fluorescent units, 3-(9*H*-carbazol-9-yl)benzonitrile (Cz-CN), a rigid axial chiral molecular ((−)-(*S*)-Cz-Ax-CN and (+)-(*R*)-Cz-Ax-CN, **(−)-(*S*)-5** and **(+)-(*R*)-5**, Fig. 3c) with a large torsion angle (64°) was constructed. The molecular architecture simultaneously features π-conjugated charge transfer (CT) and spatial CT effects, enabling excellent TADF activity and pronounced circularly polarized luminescence characteristics ($|g_{lum}| = 4.5$–4.8×10^{-3}).

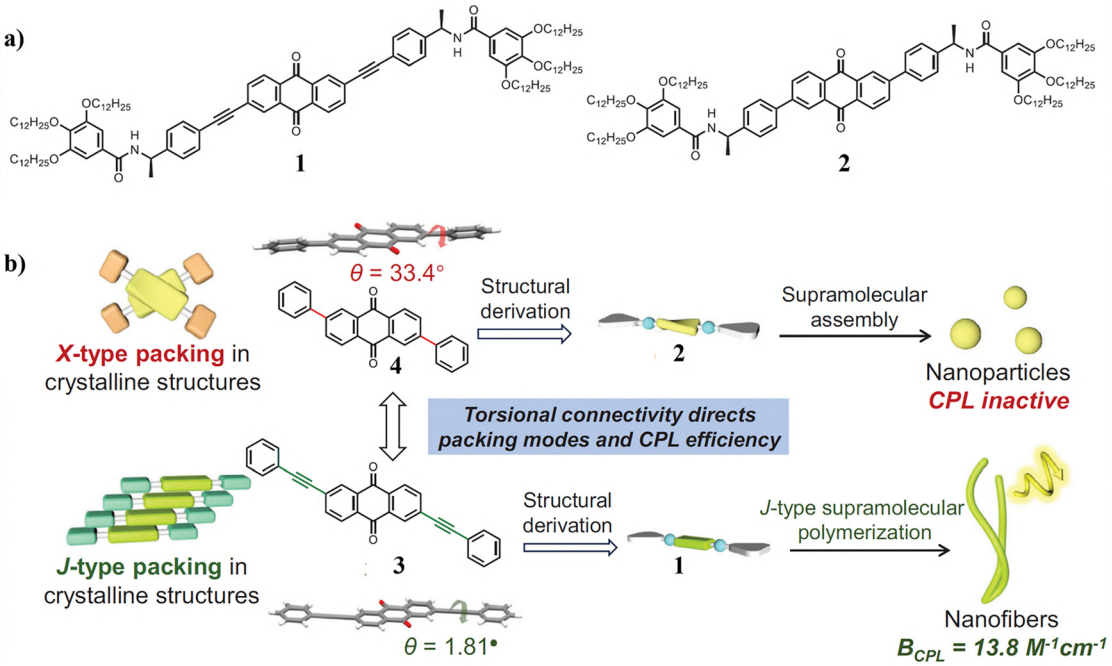

Fig. 2 (a) The chemical structures of **1** and **2**. (b) Schematic illustration of precise torsional engineering in point-chiral anthraquinones for J-type supramolecular polymerization and enhanced CPL. Reproduced with permission from ref. 30. Copyright 2025, Wiley-VCH.

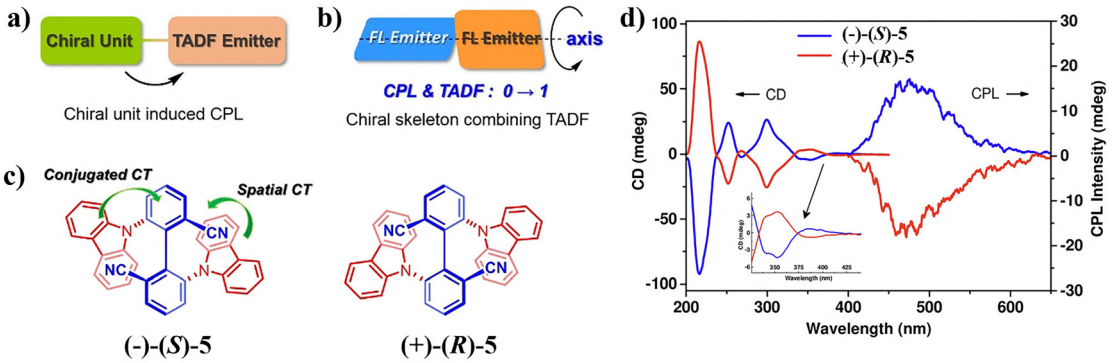

Fig. 3 (a) Chiral perturbation strategy. (b) Chiral emitting skeleton strategy. (c) Chemical structures of axial TADF enantiomers. (d) CD and CPL spectra of **(–)-(*S*)-5** and **(+)-(*R*)-5** in film states. Reproduced with permission from ref. 32. Copyright 2020, Wiley-VCH.

In 2021, Pan *et al.* reported two novel blue-emitting axially chiral biphenyl-based TADF materials, *M*-BPCZ4 and *P*-BPCZ4 (**6** and **7**, Fig. 4a).[33] These compounds achieved highly efficient circularly polarized organic light-emitting diodes (CP-OLEDs) through their rigid molecular architecture, which incorporates four carbazole donors and two cyano acceptors. Experimental results revealed that both materials exhibited significant CPL properties in toluene solution, with dissymmetry factor $|g_{PL}|$ values of 5.0×10^{-3} and 4.7×10^{-3} (Fig. 4b), respectively. Simultaneously, the positional variation of carbazole units significantly influences both the racemization temperature and CPEL performance of the materials. By reducing the distance between the chiral center and the luminescent core, the CPL signal was effectively optimized. This work provides a novel strategy for designing CP-TADF materials.

In 2021, Zuo *et al.* reported two CP-TADF materials, rod-shaped *R*/*S*-*p*-BAMCN and helical-shaped *R*/*S*-*o*-BAMCN (***R*/*S*-8** and ***R*/*S*-9**, Fig. 5a), based on a novel chiral donor (*R*/*S*-*N*2,*N*2′-diphenyl-[1,1′-binaphthalene]-2,2′-diamine, BAM).[34] Through a rigid D*–A–D* molecular architecture design, these materials demonstrate outstanding photophysical properties, achieving a maximum photoluminescence quantum yield (PLQY) of 0.86, a narrow FWHM of 38 nm in cyclohexane, and remarkable circularly polarized photoluminescence (CPPL) characteristics with $|g_{PL}|$ reaching 5.3×10^{-3} in toluene. This work provides a novel approach to developing CP-TADF materials that

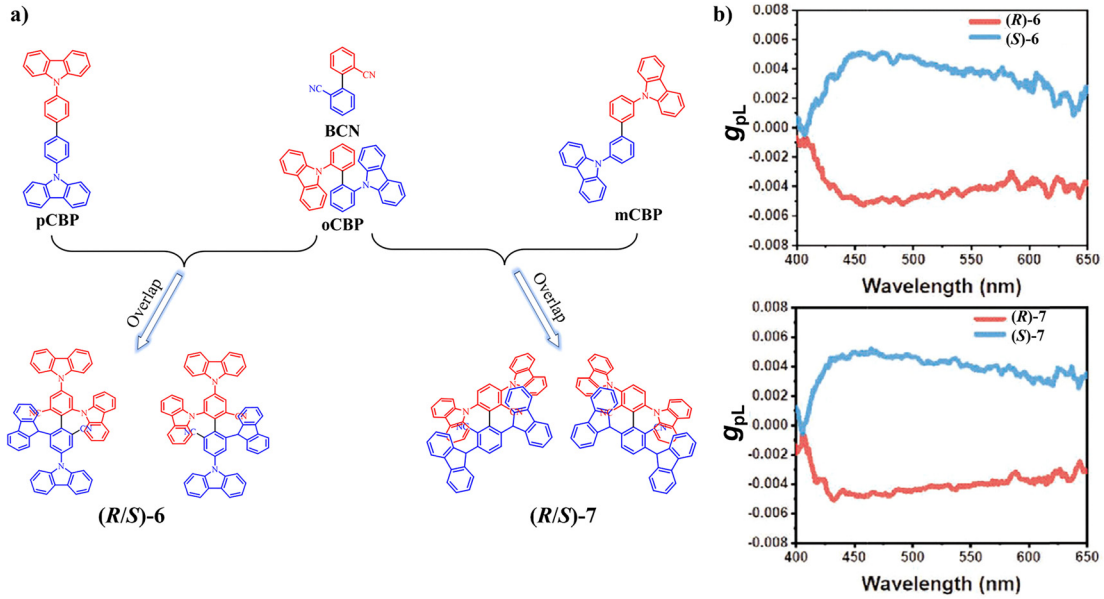

Fig. 4 (a) Design concept and molecular structures of **6** and **7**. (b) The g_{PL} *versus* wavelength curves of **(*R*/*S*)-6** and **(*R*/*S*)-7**. Reproduced with permission from ref. 33. Copyright 2021, Wiley-VCH.

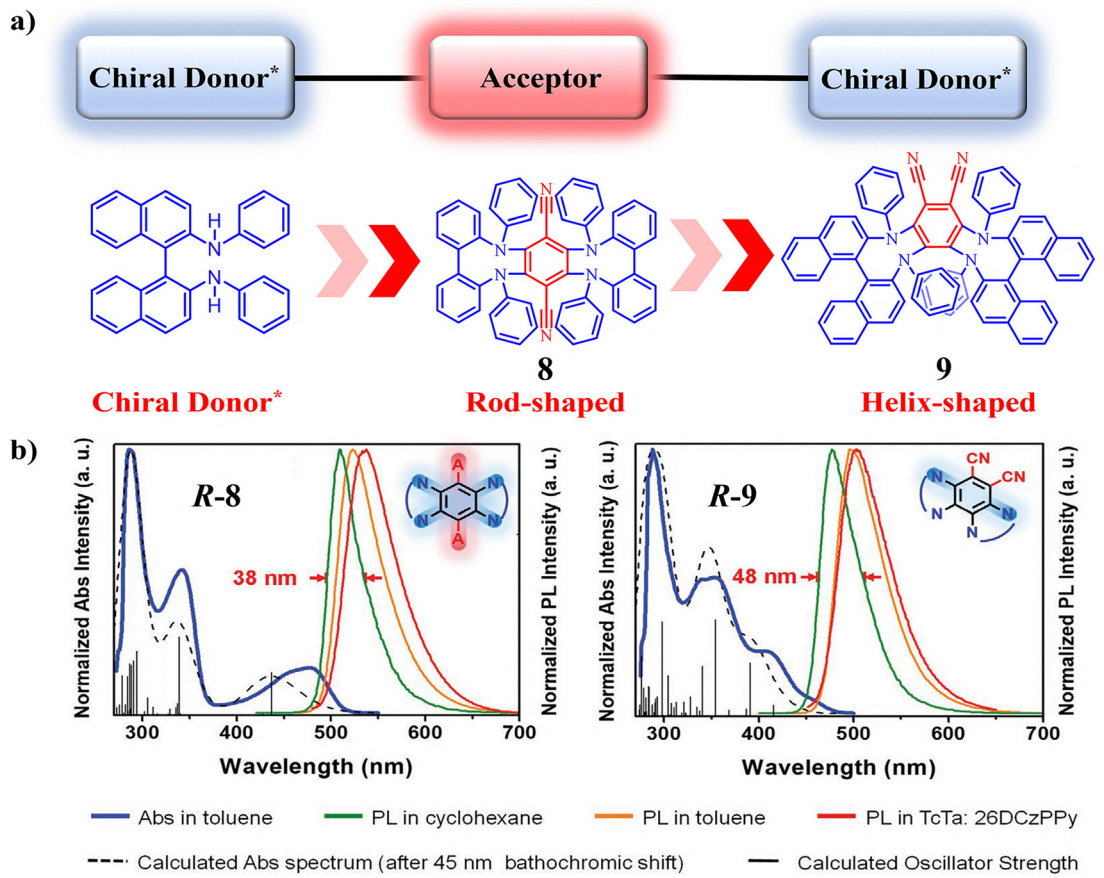

Fig. 5 (a) CP-TADF materials studied based on the D*–A–D* skeleton strategy. (b) The UV-vis absorption and PL spectra of ***R*-8** and ***R*-9**. Reproduced with permission from ref. 34. Copyright 2021, Wiley-VCH.

simultaneously achieve narrowband emission and highly efficient circularly polarized luminescence.

3.3 Planar chirality

Planar chirality is a distinct form of chirality that arises from the asymmetric arrangement of planar structures within molecular or supramolecular systems. Its defining characteristic lies not in a traditional tetrahedral carbon atom as the chiral center, but rather in the asymmetric spatial arrangement of substituents or functional groups within a planar structure. The application of planar chirality in luminescent materials is primarily manifested in the modulation of photophysical properties through the asymmetric arrangement of molecular structures.

In 2024, Lin *et al.* comprehensively summarized key breakthroughs in CPL studies of planar chiral organic compounds, systematically reviewing recent advancements in this field.[35] Research demonstrates that planar chiral macrocycles—represented by [2.2]paracyclophane, pillararene, prismarene and pagodarene systems—exhibit exceptional CPL performance through their rigid frameworks and strategic functionalization. For instance, [2.2]paracyclophane derivatives have achieved tunable emission from blue to yellow-green through molecular engineering that incorporates luminescent moieties (*e.g.*, pyrene, carbazole, and B–N heteroaromatics) into their rigid scaffolds. In 2014, Chujo *et al.* synthesized **10** (Fig. 6a) (Φ_F = 45%, $|g_{lum}| = 1.1 \times 10^{-2}$), which demonstrates exceptional solid-state CPL performance.[36] As observed, compound **11**, synthesized by Wei *et al.* in 2023, achieves a blue shift in its CPL signal through B–F coordination in the presence of fluoride ions, demonstrating dynamic modulation characteristics.[37] Through host–guest chemistry (as exemplified by the **12**@L-Ala complex synthesized by Yang *et al.* in 2022), chiral induction enhances the $|g_{lum}|$ value to 2.0×10^{-4}, expanding the application scope of supramolecular chiral engineering.[38] In 2020, Chen *et al.* designed and synthesized pagoda[4]arene (**13**, Fig. 6a) achieving stable planar chirality through rigid anthracene units, exhibiting a solid-state Φ_F of 37% and a $|g_{lum}|$ value of 5.3×10^{-3},[39] demonstrating the potential of non-traditional macrocyclic systems in solid-state luminescent devices.

Simultaneously, the regulation of planar chirality contributes to the construction of CP-TADF. CP-TADF materials are regarded as ideal candidates for CP-OLEDs due to their facile derivatization, efficient harvesting of both singlet and triplet excitons, and high device efficiency in organic molecular systems. In 2024, Zheng *et al.* designed and synthesized four CP-TADF molecules featuring a bicyclophane (DpCp) scaffold.[40] These compounds are specifically two pairs of optically pure planar chiral enantiomers (**14** and **15**, Fig. 7a) and two kinds of bridged meso compounds (**16** and **17**, Fig. 7a). These compounds exhibit emission peaks spanning the blue-green region (464–485 nm) in toluene solution, with a narrow FWHM of only 38 nm and remarkably high PLQYs reaching 93.7%, approaching the theoretical limit. Enantiomeric CP-TADF molecules (***R*/*S*)-14** and (***R*/*S*)-15** were obtained *via* chemical resolution by exploiting the asymmetry of the DpCp bridged configuration. Their CPL spectra exhibited mirror–symmetric relationships, with a $|g_{PL}|$ value of 6.4×10^{-4} in toluene solution, which increased to 6.7×10^{-4} in doped films.

3.4 Helical chirality

Carbon helicenes are a unique class of polycyclic aromatic hydrocarbons (PAHs) characterized by angularly annulated benzene rings in *ortho*-fused configurations, forming helical geometric structures. Helical structures induce intrinsic chirality in materials, enabling applications in asymmetric catalysis,[41] nonlinear optics,[42] and molecular machines.[43] Carbon helicenes have emerged as a research hotspot in luminescent materials

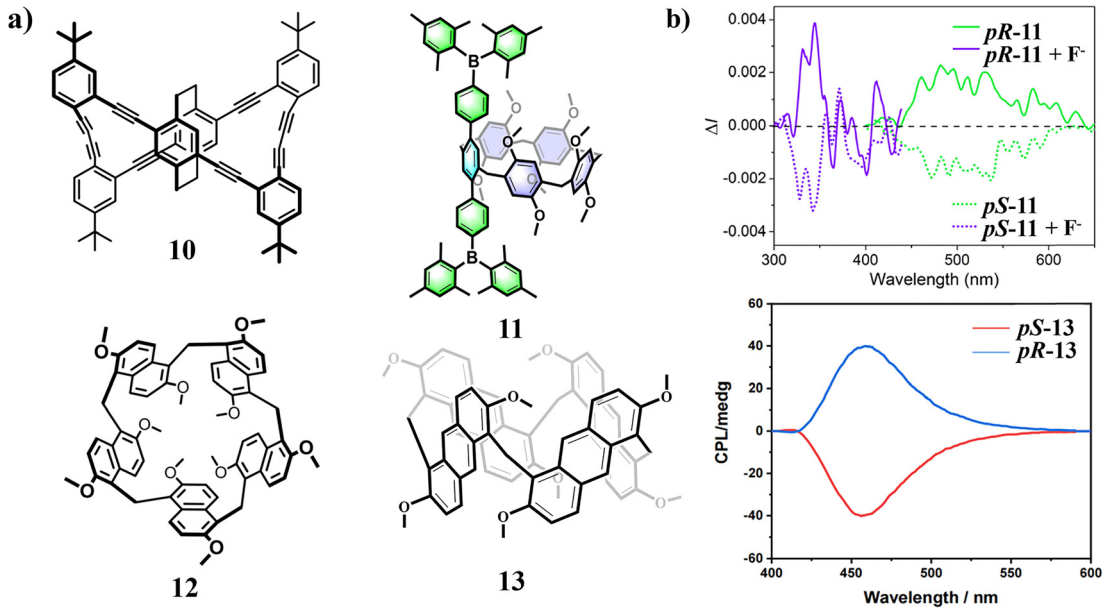

Fig. 6 (a) Schematic diagrams of **10**, **11**, **12** and **13.** (b) CPL spectral responses of enantiomers for **11** in the presence of an excess amount of fluoride ions and ***pS*/*pR*-13**. Reproduced with permission from ref. 35. Copyright 2024, Royal Society of Chemistry.

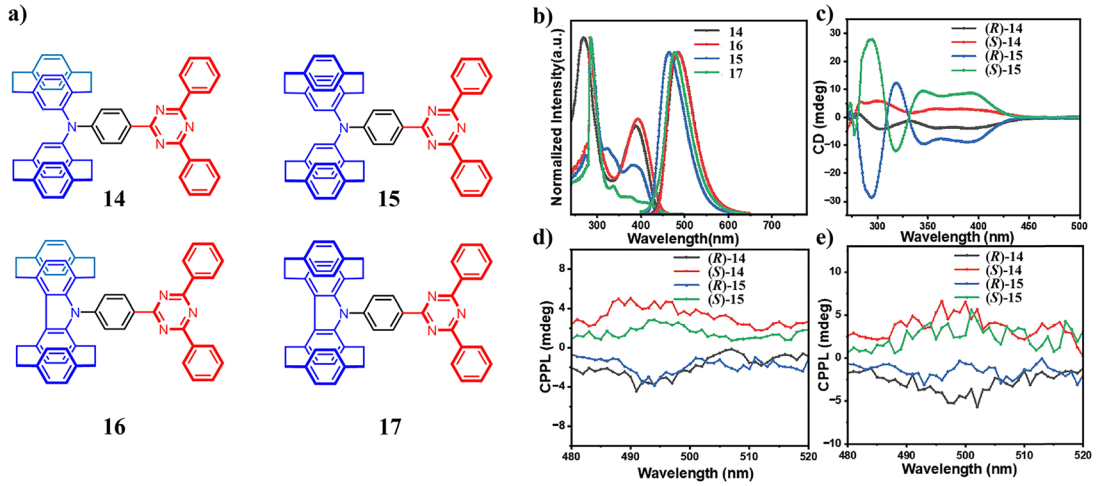

Fig. 7 (a) Schematic diagrams of **14**, **15**, **16** and **17**. (b) Normalized UV/Vis absorption and PL spectra of **14**, **15**, **16** and **17**. (c) CD of ***R*/*S*-14** and ***R*/*S*-15**. (d) CPPL spectra of ***R*/*S*-14** and ***R*/*S*-15** in toluene. (e) CPPL spectra of ***R*/*S*-14** and ***R*/*S*-15** in doped films 3 wt% in mCBP. Reproduced with permission from ref. 40. Copyright 2024, Wiley-VCH.

in recent years, particularly as high-performance CPL emitters. An ideal CPL emitter should simultaneously possess a high Φ and a large $|g_{lum}|$.[44] However, traditional carbohelicenes suffer from an inherent trade-off between the quantum yield and the luminescence dissymmetry factor. The development of novel helicene architectures with both high *g*-factors and strong CPL activity through π-extension strategies, non-planar structural construction, and heteroatom incorporation provides innovative solutions to address this challenge.

3.4.1 π-Conjugation extension. Since Newman and Lednicer first reported [6]helicene in 1956,[45] researchers have made tremendous efforts to synthesize higher [*n*]helicenes. This pursuit has been driven by the unique chiral optical properties of extended π-conjugated systems. A direct approach involves extending the π-conjugation along the helical axis of helicenes. Theoretical studies indicate that the asymmetry factor of single-handed [*n*]carbohelicenes can increase with the number of aromatic rings. The longest carbon helicene reported to date has been [16]helicene, synthesized by Fujita *et al.* in 2015,[46] which achieved only a 7% yield in the final photocyclization step. This method of increasing helical length has not been perfectly achieved, primarily due to limitations in structural stability and synthesis efficiency.[5]

Another effective method to enhance the asymmetry factor in helicene chemistry involves lateral π-conjugation extension. In 2021, Narita *et al.* reported the high-yield synthesis of π-extended [7]helicene and [9]helicene (**18** and **19**, Fig. 8a) through regioselective cyclodehydrogenation.[47] They employ a pre-fused benzene ring structure to lock critical ring positions, thereby preventing aryl rearrangement during the ring dehydrogenation process. Subsequently, **18** (76% yield) and **19** (84% yield) were synthesized with high regioselectivity under mild conditions (0 °C) using DDQ/$FeCl_3$ or DDQ/TfOH systems. Among them, **18** (Φ = 0.25) and **19** (Φ = 0.41) exhibit significantly higher quantum yields compared to non-π-extended spiroacetenes (Φ < 0.02). The absorption dissymmetry factor $|g_{abs}|$ of **19** (10.58×10^{-3}) demonstrates an approximately 10-fold enhancement compared to **18** (1.24×10^{-3}). The luminescence dissymmetry factor $|g_{lum}|$ of **19** reaches 7.4×10^{-3}, ranking among the highest values reported for carbon

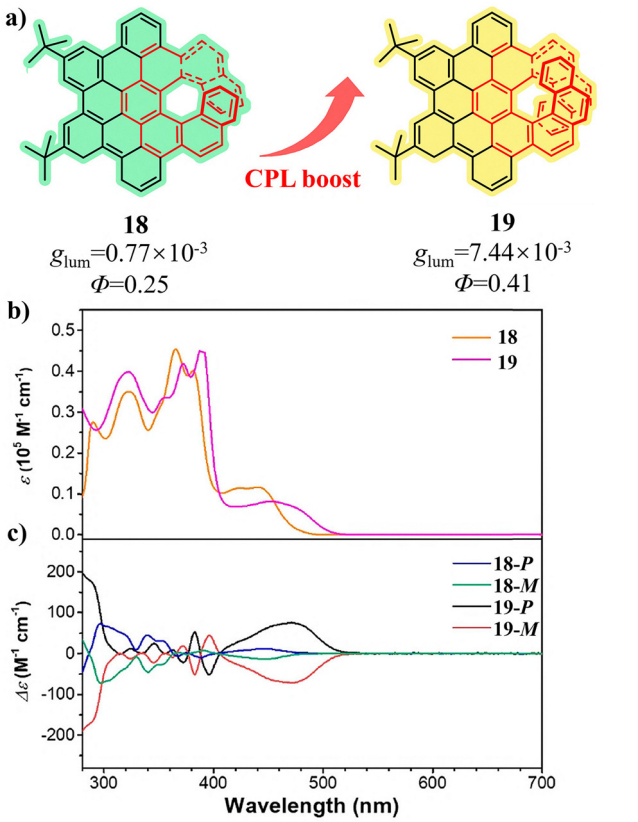

Fig. 8 (a) Schematic diagrams of **18** and **19**. (b) Absorption spectra and (c) CD spectra of **18** and **19** in THF solutions. The solution concentration is 1.0×10^{-5} M. Reproduced with permission from ref. 47. Copyright 2021, ACS Publications.

spiroacenes. The results demonstrate that elongating the spiroacene backbone and π-extension significantly enhance both the $|g_{lum}|$ and Φ.

In 2018, Campaña *et al.* constructed a fully π-extended undecabenzannulated [7]spiroacene (**20**, Fig. 9a) *via* helical arrangement of three hexabenzocoronene (HBC) units, including two saddle-shaped HBC units and one planar HBC unit.[48] Its fluorescence quantum yield in the solution state is Φ = 0.098, which is higher than that of traditional seven-layered spiroacenes ($\Phi \approx 0.014$). This material, as a chiral luminescent material, holds potential in the fields of organic electronics and photovoltaics. They also constructed a new superhelical structure in 2022.[49] This structure consists of three HBC units arranged in a helical geometry (**21**, Fig. 9a), forming two [5]spiroacenes and one [7]spiroacene. The central HBC features a convective segment that induces a saddle-helix hybrid three-dimensional structure, significantly enhancing the twist. Its emission wavelength extends to 850 nm, with $|g_{lum}| = 3.0 \times 10^{-3}$, making it the first reported near-infrared circularly polarized luminescence (NIR-CPL) superhelicene. This material exhibits a B_{CPL} of 90.5 L mol^{-1} cm^{-1}. As a high-brightness chiral luminescent material, it holds promising application prospects in organic optoelectronic devices, such as OLEDs and chiral sensors.

In 2023, Gong *et al.* synthesized a novel chiral nanographene (namely EP9H),[50] whose core fragment is pentadecylbenzo[9]spiroacene, containing four fused HBC units (**22**, Fig. 9b), with a total of 150 conjugated carbon atoms. Compared with [9]spirarene, the structural innovation of 22 lies in the complete extension of the π-system perpendicular to the helical axis. This not only constructs a longer-range conjugated network but also provides a structural foundation for efficient overlap between adjacent HBC layers. Among them, the $|g_{lum}|$ value of EP9H is 4.50 × 10^{-2}, and the B_{CPL} is 304 M^{-1} cm^{-1}. Notably, this efficient inter-HBC-layer overlap dramatically reinforces intermolecular electronic coupling. Combined with the π-extension strategy along the helical axis, EP9H achieves not only a significant red-shift of emission wavelength into the near-infrared (NIR) region after structural modification but also simultaneous improvements in Φ_F and CPL performance. This finding demonstrates that extending the conjugation length along the helical axis of the spiral π-system, while promoting efficient overlap between adjacent HBC layers through structural design perpendicular to the helical axis, constitutes a critical strategy for constructing high-performance chiral CPL molecular emitters. Additionally, helical pitch serves as a critical parameter for modulating chiroptical properties. Ravat *et al.* demonstrated that alkyl bridge length can be precisely tuned to control the helical pitch, systematically investigating its effects on optical anisotropy, chiroptical response, and electronic conjugation.[8] Their study revealed that reducing the helical pitch enhances spatial conjugation effects, thereby significantly improving the *g*, red-shifting emission wavelengths, strengthening electronic coupling, and lowering LUMO energy levels. This well-defined structure–property relationship provides a novel strategy for designing high-performance chiral organic semiconductor devices.

3.4.2 Non-planar structure construction. The curvature of nanographene is influenced by the non-hexagonal rings it contains: five-membered rings induce positive curvature (bowl-shaped), while seven or eight-membered rings induce negative curvature (saddle-shaped).[51] The introduction of non-planar structures significantly influences the chiral stability of stereocenters by disrupting molecular symmetry, restricting conformational freedom and enhancing steric hindrance

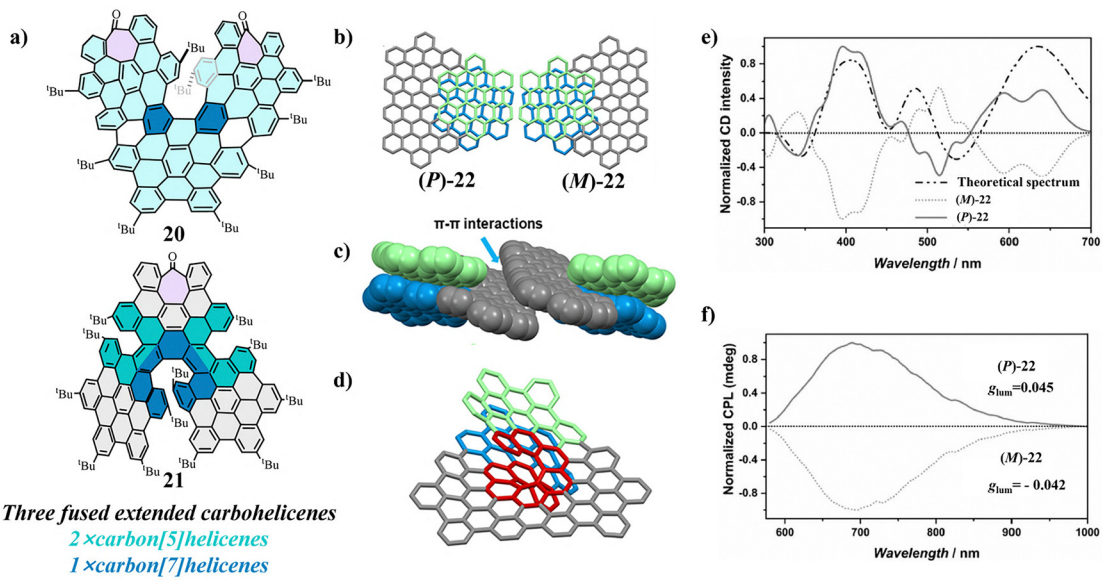

Fig. 9 (a) Schematic diagrams of **20** and **21**. Reproduced with permission from ref. 49. Copyright 2022, Royal Society of Chemistry. (b) Schematic diagram of **(*P*)-22** and **(*M*)-22**. (c) EP9H racemic dimer. (d) Core fragment (red) of **22**. (e) CD spectra of **(*P*)-22** (solid line) and **(*M*)-22** (dash line), also the simulated spectrum of **(*P*)-22** (dash line). (f) CPL spectra of **(*P*)-22** (solid line) and **(*M*)-22** (dash line). Reproduced with permission from ref. 50. Copyright 2023, Wiley-VCH.

effects. This structural modification promotes non-colinear coupling between μ_e and μ_m, thereby increasing $|g_{lum}|$.[52] Concurrently, it modifies electron–hole wavefunction overlap to optimize the singlet–triplet energy gap, resulting in synergistic enhancement of both the fluorescence quantum yield and CPL intensity.[53]

In 2020, Narita *et al.* unexpectedly synthesized a negatively curved nanographene (NG)4 through aryl rearrangement and stepwise cyclodehydrogenation reactions, featuring a structure containing two heptagonal rings and one [5]helicene unit (**23**, Fig. 10a).[54] The molecular structure was confirmed by X-ray crystallography, DFT calculations, and spectroscopic analysis to exhibit a curved span of 9.79 Å and a helical twist angle of 35.2°. Theoretical calculations revealed that the aryl rearrangement pathway, proceeding *via* radical or arenium ion intermediates, exhibits lower energy barriers compared to the helicene formation pathway, thus dominating the reaction process. This nanographene exhibits distinctive photophysical properties, including solution-state orange fluorescence (Φ_F = 11%), reversible crystalline-to-amorphous mechanochromism and mirror-image CD signals upon HPLC resolution of chiral enantiomers. This work provides a novel strategy for the controlled synthesis and optoelectronic functionalization of negatively curved nanocarbon structures.

In 2020, Campaña *et al.* synthesized a novel family of HBC-based helical nanographenes.[55] The core innovation of this work lies in the strategic incorporation of eight-membered carbon rings into π-extended carbon[5]helicene skeletons, creating highly distorted saddle-helix hybrid architectures (**24**, **25** and **26**, Fig. 11a). Experimental and theoretical studies confirmed that this material achieves an exceptional torsional angle of 79.5° while demonstrating remarkable thermal stability showing no racemization or decomposition even after 5 hours at 200 °C. Single-crystal X-ray diffraction and DFT-optimized structures show excellent agreement, revealing its unique asymmetric saddle-shaped curvature and π-extended electronic properties. This material exhibits exceptional CPL activity, with a high $|g_{lum}|$ reaching 7×10^{-4}. Simultaneously, this material achieves a maximum Φ of up to 13%, coupled with an exceptionally long excited-state lifetime of 18 ns, making it an ideal candidate for time-resolved optical techniques such as fluorescence lifetime imaging microscopy.

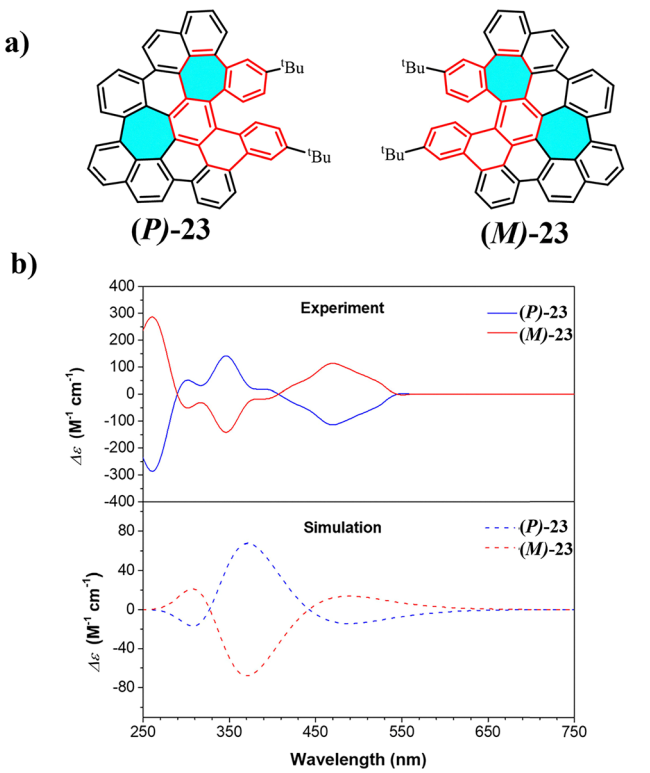

Fig. 10 (a) Schematic diagrams of (***P***)-**23** and (***M***)-**23**. (b) Experimental (solid lines) and TD-DFT simulated (dashed lines) CD spectra of (***P***)-**23** and (***M***)-**23**. Reproduced with permission from ref. 54. Copyright 2020, American Chemical Society.

In 2021, Campaña *et al.* achieved the first synthesis of a π-extended carbon[5]helicene incorporating a nine-membered ring as the helical segment, marking the first instance of a nine-membered carbon ring integrated into an HBC skeleton (**27**, Fig. 12a).[56] Single-crystal X-ray diffraction analysis confirmed that the incorporation of the nine-membered ring induces significant structural distortion, with the dihedral angle between the two terminal benzene rings reaching 134.8°. This structural configuration significantly enhances the $|g_{abs}|$, achieving a value of 4.2×10^{-3} representing a more than two-fold improvement over previous eight-membered ring analogues and demonstrating exceptional chiroptical performance. Spectroscopic and electrochemical studies reveal that the incorporation of a nine-membered ring not only widens the optical bandgap but also endows the molecule with solvent-dependent fluorescence properties. This study demonstrates the regulatory role of macrocycle size on structural rigidity and chiroptical properties, while providing a novel strategy for designing highly distorted yet rigid chiral nanocarbon materials.

In 2023, Feng *et al.* reported the precision synthesis of the first helical bilayer non-benzenoid nanographene featuring a [10]helicene scaffold with two embedded heptagonal rings (**28**, Fig. 13a).[57] Constructing efficiently through the Scholl reaction of a pre-designed azaarene precursor, HBNG1 exhibits a distinctive bilayer-twisted architecture. Single-crystal X-ray analysis reveals an exceptionally small interlayer distance of merely 3.2 Å – the shortest reported for such molecular systems and demonstrates intramolecular through-space conjugation effects. Furthermore, the enantiomers obtained through chiral resolution exhibit electronic circular dichroism (ECD) and CPL responses, with a maximum $|g_{abs}|$ value reaching 6.6×10^{-3} and $|g_{lum}|$ achieving 1.3×10^{-3}. This study provides novel design principles for non-benzenoid multilayer nanographenes and opens new avenues for their applications in chiral optoelectronics.

3.4.3 Heteroatom incorporation. The introduction of heteroatoms into carbon helicenes represents an alternative strategy for modulating their electronic properties, stability, and chiral activity, thereby significantly expanding their applications in CPL, optoelectronics, and catalysis.[58]

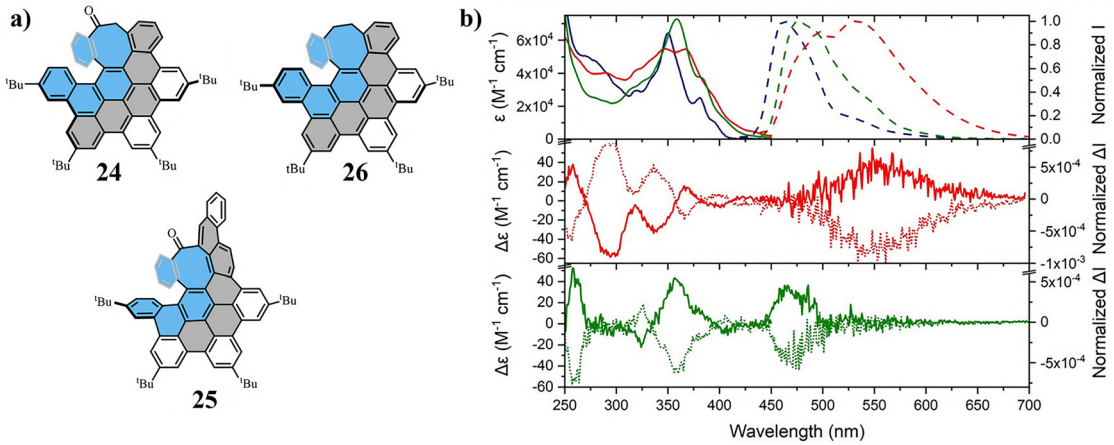

Fig. 11 (a) Schematic diagrams of **24**, **25** and **26**. (b) Top: UV/Vis absorption spectra (solid line) and fluorescence spectra (dashed line) of **24** (green), **25** (red), and **26** (blue). Middle/bottom: ECD spectra (left, 250–450 nm) and CPL spectra (right, 450–700 nm) of **24** (bottom) and **25** (middle) in CH_2Cl_2 at rt. First, P (solid line) and second, M (dashed line) (CSP)HPLC eluted fractions. Reproduced with permission from ref.55. Copyright 2021, Wiley-VCH.

In 2018, Jux *et al.* reported the synthesis of a new type of π-extended helical chromophore based on HBC.[59] This study achieved the synergistic integration of heteroatom functionalization and π-conjugation extension through an oxidative cyclization strategy to incorporate oxygen atoms into the HBC framework, coupled with cascade reactions to construct a helical architecture.

In 2021, Zhang *et al.* successfully embedded a seven-membered nitrogen heterocycle and an eight-membered nitrogen heterocycle into the fjord regions of HBC skeletons, respectively, through a combination of the Diels–Alder reaction, Suzuki–Miyaura coupling, and Scholl-type cyclodehydrogenation.[60] This strategy yielded two nitrogen-doped hexabenzocoronene-based nanographenes (**29** and **30**, Fig. 14). Among them, **29** adopts a saddle-shaped curvature, while **30** forms a saddle-helix hybrid conformation due to the distortion of the eight-membered ring, with its [5]helicene fragment exhibiting a torsional angle of 36°. This work achieves the first precise embedding of nitrogen-doped medium-sized rings into the HBC framework, offering a novel strategy for modulating the topological structures and optoelectronic properties of nanographenes.

3.5 Cage chirality

The concept of cage chirality originated from in-depth understanding of three-dimensional symmetry breaking in molecular structures. In 1994, Böhmer *et al.* first observed "inherent

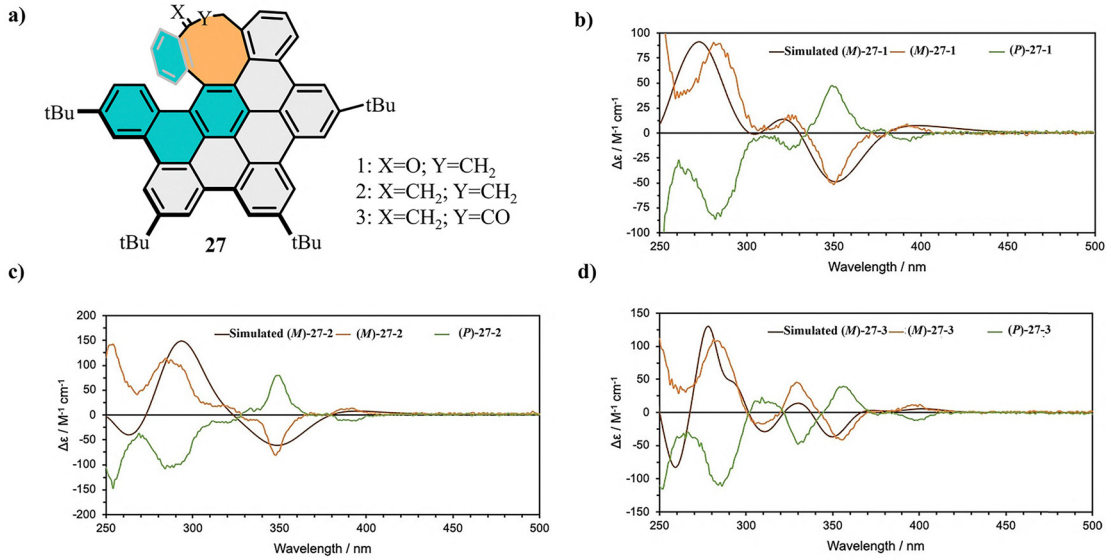

Fig. 12 (a) Schematic diagram of **27**. (b)–(d) Experimental ECD spectra of ***(M/P)*-27-1** to ***(M/P)*-27-3** in DCM, and simulated (CAM-B3LYP/6-311++G(d,p), IEFPCM DCM) ECD spectra of ***(M)*-isomers**: (b) ***(M)*-27-1** and ***(P)*-27-1** (orange and green, both 1.2×10^{-5} M), (c) ***(M)*-27-2** (orange, 1.0×10^{-5} M) and ***(P)*-27-2** (green, 1.1×10^{-5} M) and (d) ***(M)*-27-3** (orange, 1.3×10^{-5} M) and ***(P)*-27-3** (green, 1.4×10^{-5} M). Reproduced with permission from ref. 56. Copyright 2021, Wiley-VCH.

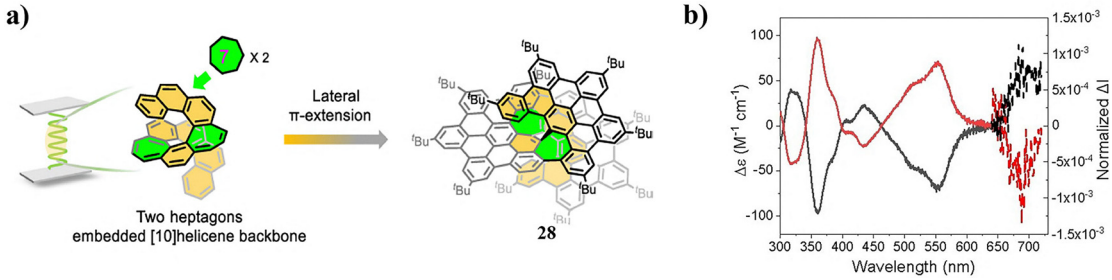

Fig. 13 (a) Schematic diagram of **28**. (b) Experimental ECD spectra (solid line) and experimental CPL spectra (dashed line, irradiation at 525 nm) of ***P*-28** (red) and ***M*-28** (black) (DCM at *ca.* 1.6×10^{-5} M and 1.2×10^{-5} M of ***P*-28** and ***M*-28**, respectively). Reproduced with permission from ref. 57. Copyright 2023, Wiley-VCH.

chirality" in calixarene frameworks, where asymmetric substitution patterns render the entire molecule chiral due to the absence of symmetry elements, resulting in non-superimposable mirror-image configurations. This discovery laid the foundation for chirality studies in cage-shaped molecular structures.[61]

In 2019, Yan *et al.* achieved a breakthrough in CPL research. For the first time, they successfully constructed a pair of enantiopure rare-earth tetrahedral cages through a chiral auxiliary ligand-induced strategy.[62] This study reports the synthesis and optical properties of a novel chiral europium tetrahedral cage $(Eu_4L_4)(R/S\text{-BINAPO})_4$ (**31**, Fig. 15). Through a chiral auxiliary ligand-induced strategy, stereochemical control of enantiopure lanthanide tetrahedral cages was achieved for the first time. The cage exhibits intense CPL with a $|g_{lum}|$ value reaching 0.20, while simultaneously setting a record for the highest luminescence quantum yield (QY = 81%) among chiral lanthanide complexes. This study further revealed a chiral memory effect: upon replacing chiral BINAPO with achiral DPEPO, the initial chiral configuration of the cage was retained, generating new enantiomers (**32**, Fig. 15) that maintained a QY of 68% with a $|g_{lum}|$ of 0.11. Their high quantum yield and strong CPL properties provide new insights for chiral sensing, bioimaging, and optical devices, while pioneering an innovative pathway for low-cost fabrication of high-performance chiral lanthanide materials.

In 2022, Zhang *et al.* reported the efficient synthesis of a pair of chiral emissive porous organic cages and their multifunctional characteristics.[63] They achieved the construction of cage architectures through a [3+6] imine condensation reaction between tetraphenylethylene derivatives and chiral diaminocyclohexane (**33**, Fig. 16a) ultimately obtaining high yields of

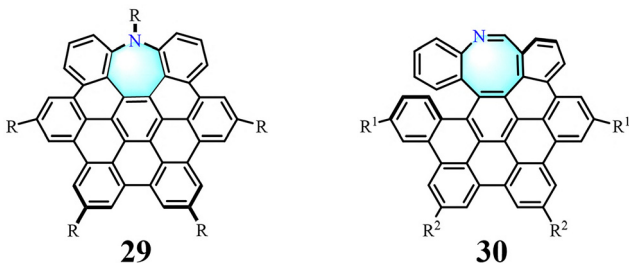

Fig. 14 Schematic diagrams of **29** (R = Me) and **30** (R^1 = Me, R^2 = *t*-Bu). Reproduced with permission from ref. 60. Copyright 2021, Wiley-VCH.

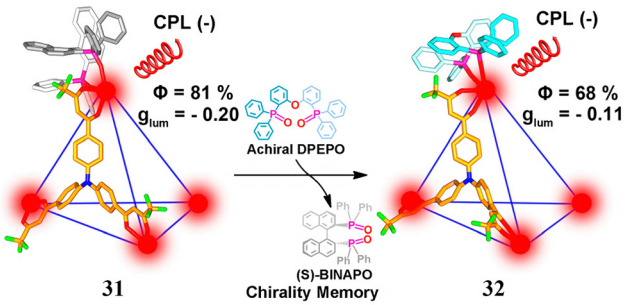

Fig. 15 Schematic diagrams of **31** and **32**. Reproduced with permission from ref. 62. Copyright 2019, Wiley-VCH.

83–91%. The point chirality of the chiral diamine induces facial chirality in the TPE units through intramolecular transfer, endowing the cage with CPL properties, leading to $|g_{lum}|$ ranging from 1.4×10^{-3} to 3.8×10^{-4}. The cage exhibits blue fluorescence emission (λ = 465 nm) in solution with a quantum yield of 22–25%, while the solid state demonstrates enhanced quantum yield (~60%) and a fluorescence lifetime of approximately 3.2 ns. This study pioneers a one-step synthetic strategy to integrate chirality, luminescence, and porosity into a single organic cage for the first time, establishing a novel multifunctional platform for chiral separation, optical materials, and molecular recognition.

4. Chiroptoelectronic application

Significant progress has been achieved in the applications of chiral carbon materials in the field of CPL in recent years. Due to their unique structural tunability and excellent optical properties, chiral carbon materials hold great potential in fields such as optoelectronic devices, 3D displays, and information encryption.

4.1 Circularly polarized organic light-emitting diodes

Chiral carbon materials induce cooperative orientation of μ_e and μ_m during electronic transitions through helical/twisted configurations at the molecular or supramolecular level, thereby generating CPEL.

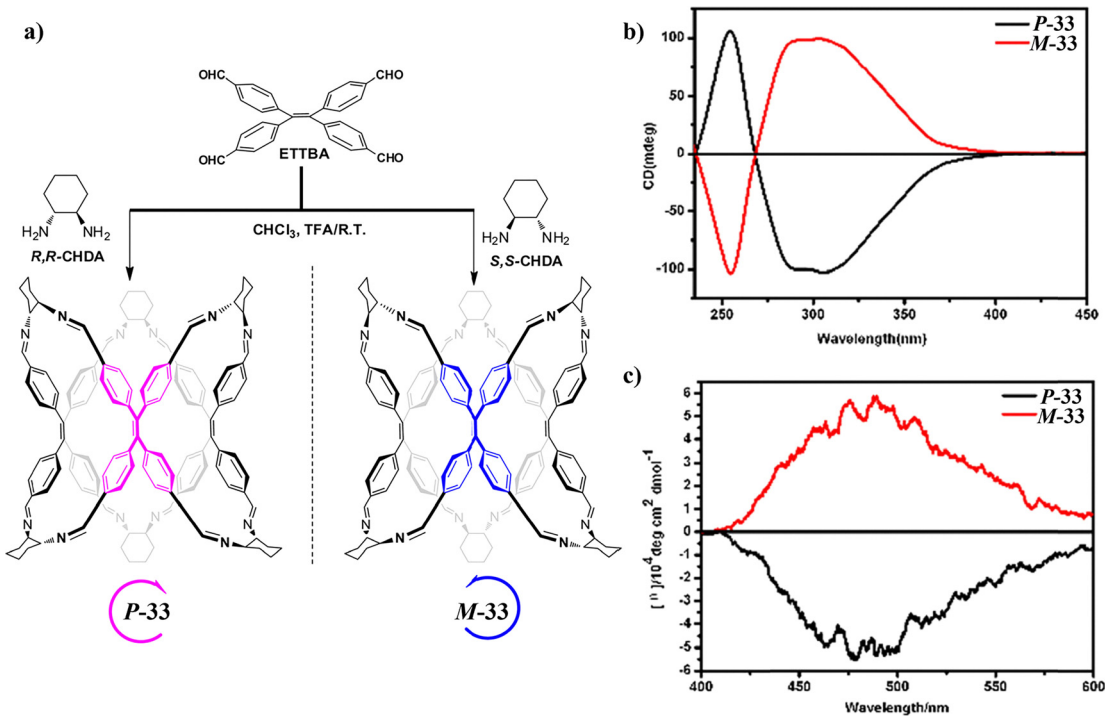

Fig. 16 (a) Schematic diagram of **33**. (b) CD spectra of ***P*-33** and ***M*-33** (solvent: CH_2Cl_2). (c) Smoothing CPL spectra of ***P*-33** and ***M*-33**. Reproduced with permission from ref. 63. Copyright 2023, Royal Society of Chemistry.

The CP-OLED devices based on **5** exhibit efficient blue electroluminescence with a maximum external quantum efficiency (EQE) of 12.5–12.7% (Fig. 17b) and an emission peak at 468 nm, while simultaneously achieving strong circularly

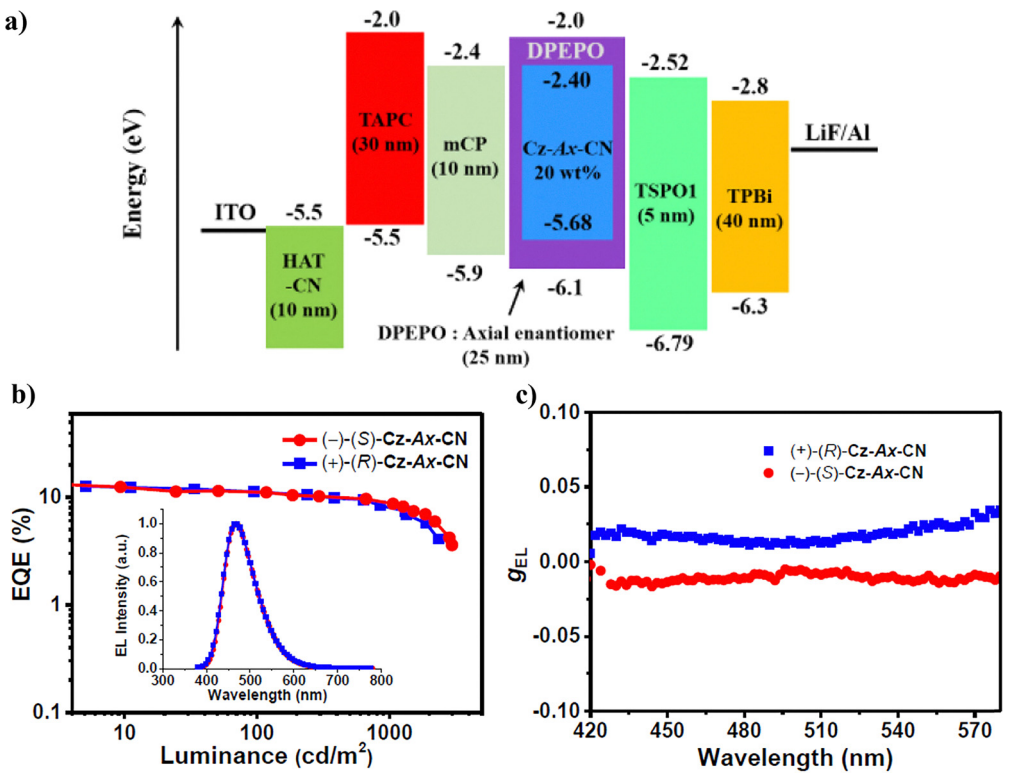

Fig. 17 (a) The energy diagram of CP-OLEDs based on **(−)-(*S*)-5** and **(+)-(*R*)-5**. (b) EQE–luminance characteristics. Inset: EL spectra of the devices at 6 V. (c) The g_{EL} values of the devices as a function of emission wavelength. Reproduced with permission from ref. 32. Copyright 2020, Wiley-VCH.

polarized electroluminescence with a electroluminescence dissymmetry factor ($|g_{EL}|$) of $\pm$1.2–1.4 $\times$ 10^{-2} (Fig. 17c).[32] This breaks through the limitation of traditional chiral perturbation strategies where the chiral unit being far from the emissive center leads to a low asymmetry factor. However, critical assessment reveals that this device suffers from efficiency roll-off. The EQE drops to 11.1% at 100 cd m^{-2} and further declines to 8.8% at 1000 cd m^{-2} (Fig. 17b). This roll-off presents a critical issue that must be overcome in real-world display applications since it severely limits the device's performance under high-brightness conditions. Moreover, the gap between the g_{EL} value and target application requirements, and, critically, the lack of operational lifetime and stability data collectively constitute key challenges requiring prioritized research and resolution.

In 2021, when Pan *et al.* employed **6** and **7** as emitters in blue CP-OLED devices, these two CP-TADF materials (D-PR and D-MR) achieved maximum EQEs of 16% and 18% (Fig. 18a).[33] Among these materials, (***R*/*S*)-6** demonstrated superior chiral thermal stability and more pronounced CPEL characteristics in device fabrication, achieving an electroluminescence dissymmetry factor $|g_{EL}|$ of 5.5 $\times$ 10^{-3} (Fig. 18b). Despite representing a significant advancement at 5.5 $\times$ 10^{-3}, this value remains orders of magnitude lower than the required $|g_{EL}| > 0.1$ for filterless 3D displays. Additionally, the device's emission peak at 480 nm falls within the sky-blue spectrum rather than the deep-blue range, both of which are core challenges for future practical applications.

The OLEDs based on **14**, **15**, **16** and **17** achieved a maximum EQE of 19.5% (Fig. 19a), while the circularly polarized OLED (CP-OLED) devices exhibited a $|g_{EL}|$ value of 7.6 $\times$ 10^{-4}.[40] This performance represents the current benchmark for all-organic CP-TADF systems. This performance demonstrates outstanding results in the field of current fully organic CP-TADF systems. However, critical challenges persist in this technology today, including limited spectral coverage (particularly the inability to tune deep-blue emission), severe efficiency roll-off and low $|g_{EL}|$ values. Future research should prioritize the design of materials with high exciton utilization efficiency and strong chiral amplification to synergistically optimize device efficiency and $|g_{EL}|$ values, while extending emission to shorter wavelengths. This approach will accelerate the industrial application of 3D displays.

In 2025, Friend *et al.* successfully developed a CP-OLED based on chiral supramolecular semiconductor thin films.[64] The chiral molecule *S*-3,7-dimethyloctyltriazatruxene (*S*-TAT, **34**, Fig. 20a) is doped as a guest into non-chiral host materials (CBP or DCzDCN) *via* vacuum co-sublimation. Thermal-triggered nano-phase separation induces *in situ* chiral crystallization, forming a helical π–π stacked structure with a pitch of 2.3 nm

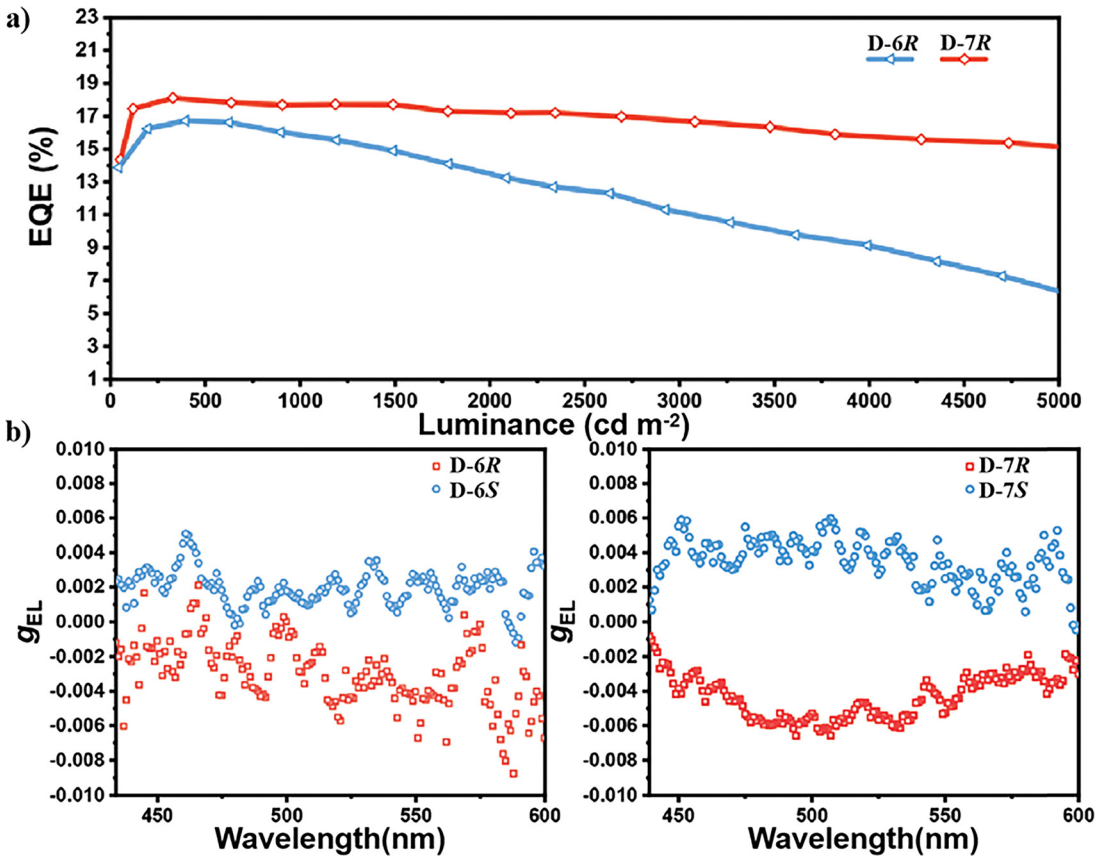

Fig. 18 (a) EQE luminance curves. (b) g_{EL}–wavelength curves of circularly polarized organic light-emitting diodes (CP-OLEDs) based on (***R*/*S*)-6** and (***R*/*S*)-7**. Reproduced with permission from ref. 33. Copyright 2021, Wiley-VCH.

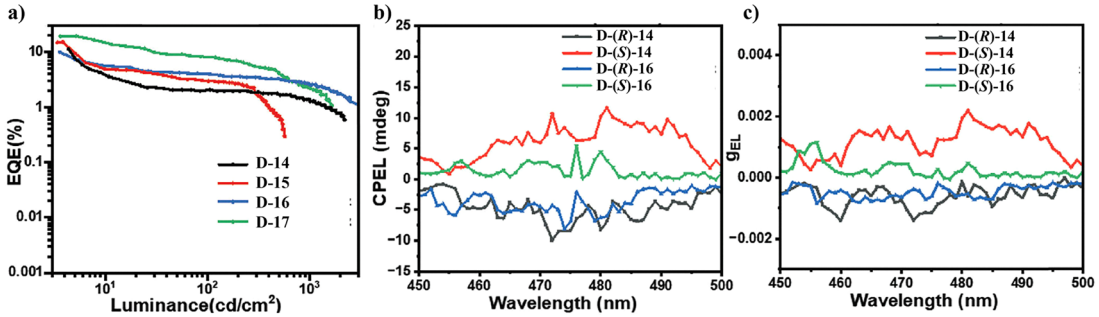

Fig. 19 (a) EQE luminance curves of the OLEDs. (b) CPEL spectra and (c) g_{EL}–wavelength curves of CP-OLEDs. Reproduced with permission from ref. 40. Copyright 2024, Wiley-VCH.

(six molecules per helical turn). This supramolecular assembly imparts orbital angular momentum to the energy bands, generating significant CPEL, while achieving a device EQE of 16% and luminance exceeding 57 000 cd m^{-2}. Currently, controllable phase separation, efficiency roll-off and stability deficiencies remain core barriers to industrialization. Band engineering should be considered together with kinetic regulation to synergistically optimize supramolecular ordering, spectral range, and fabrication processes, thereby advancing the practical implementation of chiroptoelectronics.

4.2 Sensing and detection technology

Due to the asymmetry in their molecular structure, chiral carbons achieve highly selective detection in sensing technologies by specifically recognizing enantiomers of chiral molecules. The principle relies on the stereo-matching interaction between chiral carbon materials and target molecules, distinguishing molecular configurations through signal differences such as optical, electrochemical, or mass variations.

In 2018, Miao *et al.* designed a class of functionalized hexabenzoperylene (HBP, **35**, Fig. 21a) derivatives,[65] whose twisted conformation forms a 'brickwork-like' π-stacking structure in the solid state, positioning the functional groups outside the π-stacked layers. This enables surface functionalization without compromising charge transport performance. Based on this design, the constructed supramolecular sensing platform, integrated with a microfluidic-transistor hybrid device, achieved highly sensitive and selective detection of fluoride ions in water (Fig. 21c). This work provides an innovative strategy of ''functionalization without compromising charge transport'' for organic semiconductor sensing. Improving aqueous-phase stability and simplifying device design could further advance the transition from proof-of-concept demonstrations to on-site rapid detection.

In 2025, Yuan *et al.* achieved discrimination of amino acid enantiomers through the synthesis of chiral porous organic cages (CPOCs).[66] By employing chiral pillar[4]arene derivatives as precursors, the team constructed CPOCs (**CPOC-P36** and **CPOC-M36**, Fig. 22a) with supersized chiral cavities. The CD signals aligned with the chiral inheritance of the chiral cavities, demonstrating a 6.47-fold stronger fluorescence enhancement effect for L-A1 compared to D-A1 (Fig. 22b). This enables visual

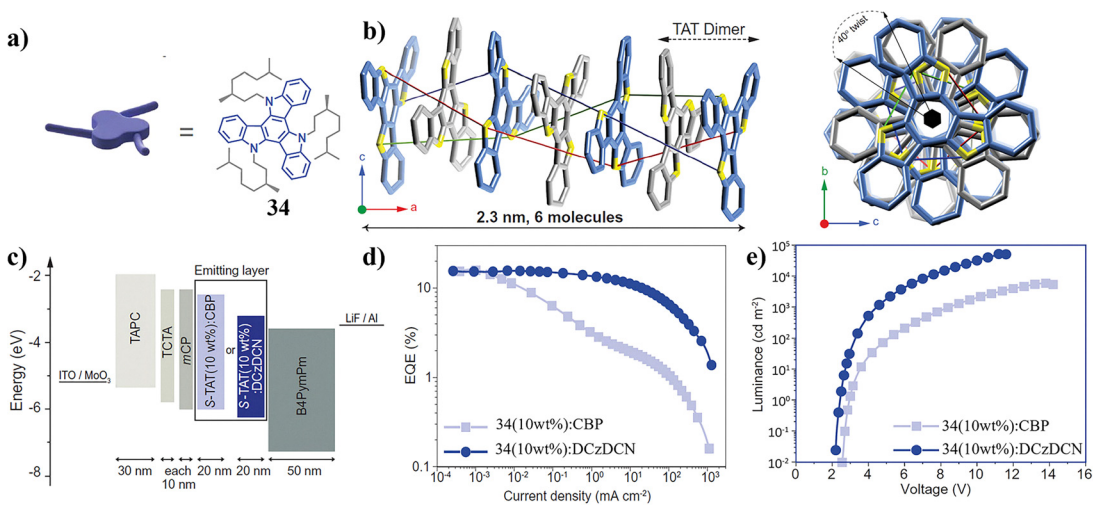

Fig. 20 (a) Schematic diagram of **34**. (b) Crystal structure of **34**. (left) Viewed along the *b* axis of the unit cell. (right) View along the axis of the unit cell. (c) Device architecture for the fabrication of CP-OLEDs using vacuum sublimation. (d) and (e) EQE *versus* current density curves and luminance *versus* voltage curves for devices using **34** (10 wt%): CBP (light-blue) and **34** (10 wt%): DCzDCN (dark blue) emitting layers. Reproduced with permission from ref. 64. Copyright 2025, American Association for the Advancement of Science.

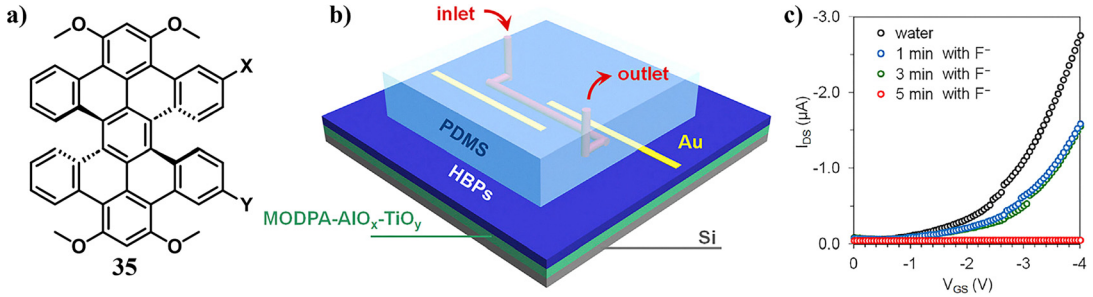

Fig. 21 (a) Schematic diagram of **35** (X = $-(CH_2)_3CH_3$, Y = $-(CH_2)_4OSi(CH_3)_3$). (b) Schematic drawing of the sensor combining a microchannel and a transistor channel of functionalized HBPs. (c) Transfer *I*–*V* curves for the thin-film transistor of **35** as measured under deionized water and under an aqueous solution of KF (1 mM) for a certain period of time. Reproduced with permission from ref. 65. Copyright 2018, Elsevier.

detection of amino acid enantiomers, thereby pioneering novel pathways for chiral separation and biosensing applications. However, synthetic inefficiency, aqueous instability, and undeveloped separation functionality severely constrain its industrial deployment.

4.3 Information encryption and anti-counterfeiting

Chiral carbons leverage their asymmetric molecular structure to achieve high-security functionalities in information encryption and anti-counterfeiting through unique CPL responsive characteristics. The underlying principle lies in the ability of chiral carbon materials to selectively absorb or emit specific CPL with defined helicity (*e.g.*, left-handed or right-handed). By designing multilayer chiral structures or dynamic responsive systems, encrypted information can be selectively visualized only under specific polarized light illumination or dynamically altered in response to environmental conditions, forming an 'optical cryptographic code'.

The ultra-thin chiral covalent organic framework (COF) nanosheets were developed by Zhang *et al.* in 2025.[67,68] The *R*-chirCOFilm (***R*-37**, Fig. 23a) with strong CPL activity was successfully prepared through a UV light-initiated chiral cross-linking reaction. Based on its photochromic properties and anti-counterfeiting patterns, flexible devices (***R*-37/PDMS**, Fig. 23d) were developed. This work establishes a new paradigm for chiral porous thin-film materials. Future efforts should prioritize intrinsic chirality enhancement and low-temperature reversible system development to advance their practical implementation in photonics and sensing applications.

In 2025, Chen *et al.* reported a photochromic chiral ionic hydrogen-bonded organic framework (***R*/*S*-IHOF-38**) with dual responsiveness to temperature and solvent, synthesized *via* a charge-assisted strategy (Fig. 24a).[69] This material exhibits significant photochromic behavior under low-temperature (−20 °C) and UV light (365 nm) irradiation, along with excellent CPL properties. Additionally, the independent hydrogen-bonding channels formed by solvent molecules (water and methanol) provide pathways for photoinduced electron transfer, enabling on–off switching of photochromism. However, transient photochromism, low

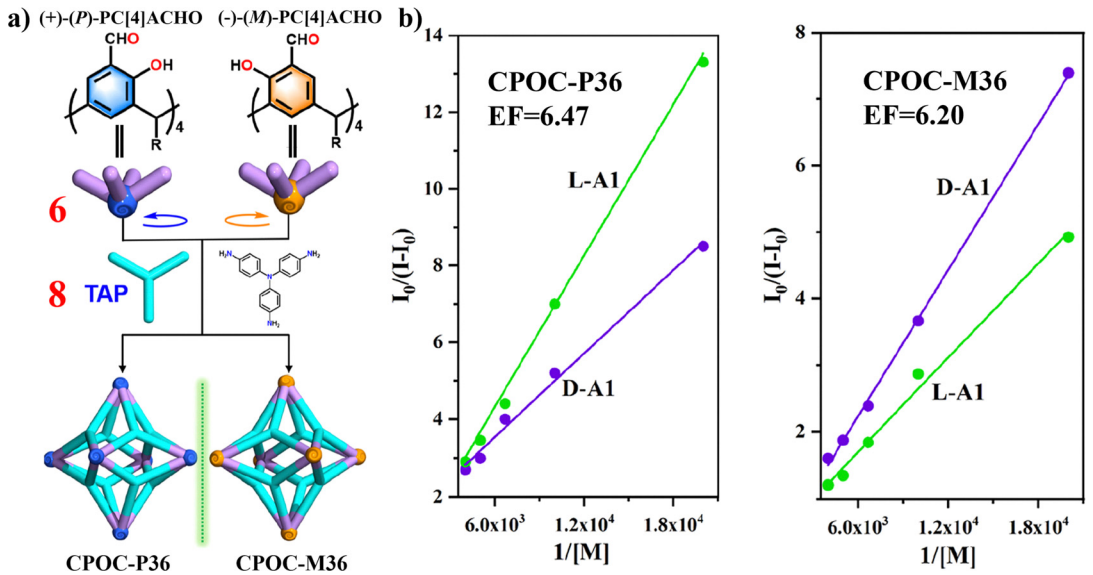

Fig. 22 (a) Schematic of [6+8] addition to obtain octahedral CPOCs (**CPOC-P36** and **CPOC-M36**). (b) Benesi–Hildebrand plots of **CPOC-P36** and **CPOC-M36** titration with D-phenylalanine and L-phenylalanine (D/L-A1). Reproduced with permission from ref. 66. Copyright 2025, American Chemical Society.

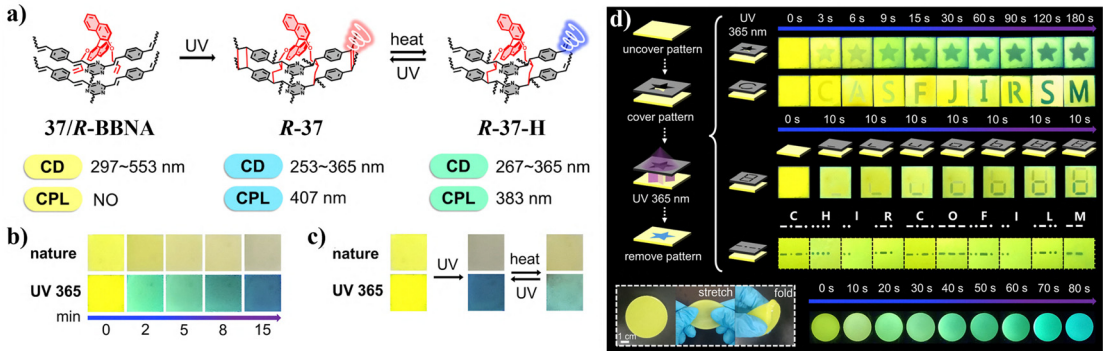

Fig. 23 (a) Structural diagrams of the **37/*R*-BBNA**, ***R*-37** and ***R*-37-H** samples with CD and CPL changes. (b) Natural light and 365 nm UV photographs of **37/*R*-BBNA** irradiated at different times in a 365 nm UV light. (c) Natural light and 365 nm UV photographs of **37/*R*-BBNA**, ***R*-37** and ***R*-37-H**. (d) Photopatterns of ***R*-37** under a 365 nm UV light and photographs of the ***R*-37/PDMS** flexible film under a 365 nm UV light. Reproduced with permission from ref. 67. Copyright 2025, American Chemical Society.

CPL dissymmetry factors, and stringent temperature control requirements remain core barriers to industrialization. While limited by current performance, this work has pioneered innovative design strategies for chiral smart materials.

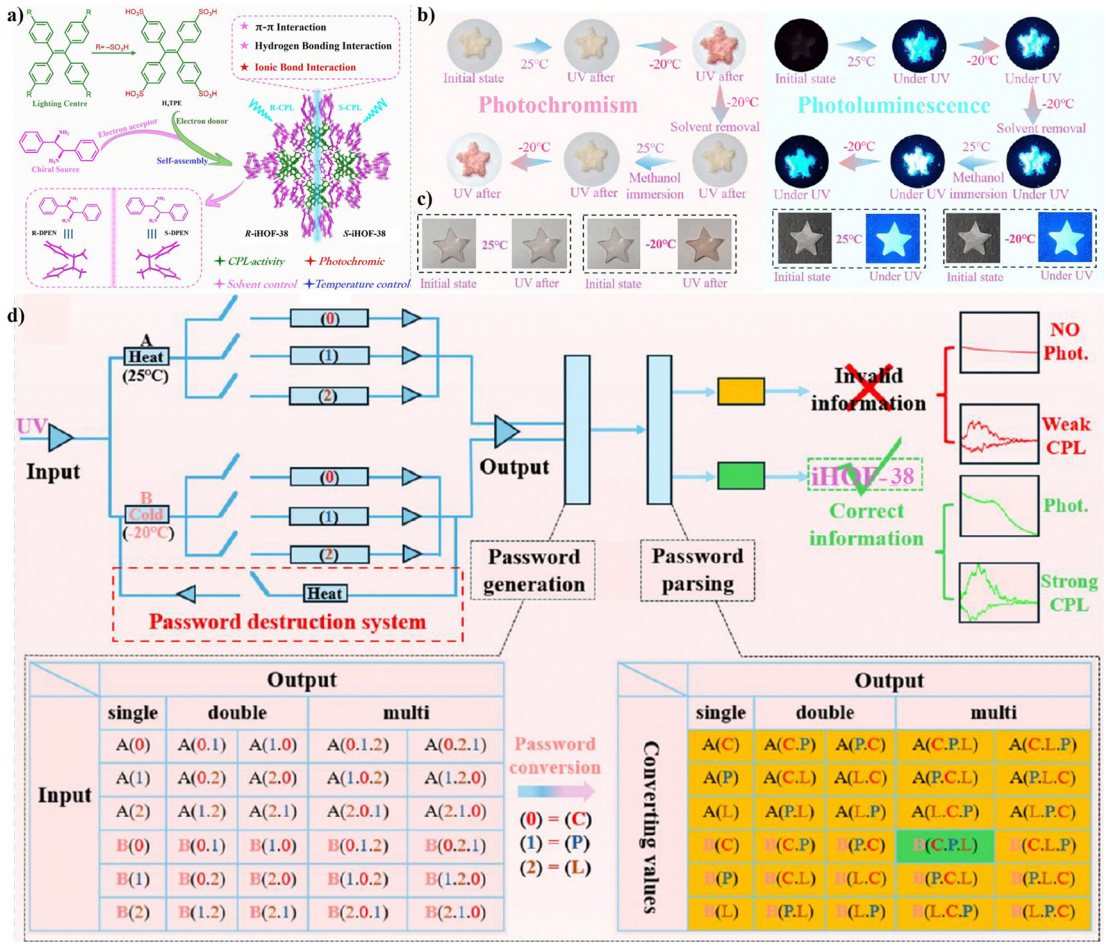

Fig. 24 (a) Chromophore tetrakis(4-sulfophenyl)ethylene (H4TPE), chiral source building blocks *R*/*S*-DPEN and ***R*/*S*-iHOF-38** constructs and supramolecular structures. (b) Photographs of the discoloration process under UV (365 nm), temperature-gated and solvent-controlled as well as fluorescence at different temperatures. (c) Photographs of discoloration and fluorescence of PVA composite films under UV (365 nm) conditions at different temperatures. (d) A multiple stimulus information encryption logic system was designed using UV = 365 nm as the stimulus source. Reproduced with permission from ref. 69. Copyright 2025, Wiley-VCH.

Table 1 Summary of the key parameters and application areas of major chiral carbon materials

Materials	$\lvert g_{lum}\rvert$	Φ_{PL}	Applications
(*R*/*S*)-**6**[33]	5.0×10^{-3} (toluene solution)[a]	0.64 (doped films)[b]	3D display terminals and high-efficiency blue-light devices
(*R*/*S*)-**7**[33]	4.7×10^{-3} (toluene solution)[a]	0.76 (doped films)[b]	3D display terminals and high-efficiency blue-light devices
(*R*/*S*)-**8**[34]	0.3×10^{-3} (toluene solution)[c]	0.86 (doped films)[d]	CP-OLED
(*R*/*S*)-**9**[34]	5.3×10^{-3} (toluene solution)[c]	0.77 (doped films)[d]	CP-OLED
18[47]	7.7×10^{-4} (THF solution)[e]	0.25 (THF solution)[e]	CPL-OLEDs and bioimaging
19[47]	7.4×10^{-3} (THF solution)[e]	0.41 (THF solution)[e]	CPL-OLEDs and bioimaging
(*P*)-**22**[50]	4.5×10^{-2} (CH_2Cl_2 solution)[f]	0.10 (CH_2Cl_2 solution)[f]	CPL devices and information-encrypted transmission
28[57]	1.3×10^{-3}	0.32% (CH_2Cl_2 solution)[g]	Spintronics and chiroptical sensing
31[62]	0.2 (CH_2Cl_2 solution)[h]	0.81 (CH_2Cl_2 solution)[h]	Advanced display technology
32[62]	0.11 (CH_2Cl_2 solution)[h]	0.68 (CH_2Cl_2 solution)[h]	Biosensing and probes
34[64]	0.24 (crystalline state)	0.58 (crystalline state)	CP-OLED, chiral exciton spin control and optical anti-counterfeiting

[a] 3×10^{-4} mol L^{-1}. [b] Dopants: diphenyl-4-triphenylsilylphenyl-phosphine oxide (25 wt%). [c] 5×10^{-5} mol L^{-1}. [d] Dopants: 4,4′,4′-tris(carbazol-9-yl)triphenylamine (8 wt%, 10 nm)/dopants: 2,6-bis-(3-(carbazol-9-yl)phenyl)pyridine (8 wt%, 10 nm). [e] 1×10^{-5} mol L^{-1}. [f] 5×10^{-6} mol L^{-1}. [g] 1.3×10^{-3} mol L^{-1}. [h] 2.5×10^{-6} mol L^{-1}.

5. Conclusions and outlook

In summary, molecular carbon materials exhibit unique optical activity, high functionalizability, and broad application potential. The development of chiral carbon allotropes has opened new avenues in molecular chemistry, particularly in optical devices, nanotechnology, and asymmetric catalysis. Advances in molecular synthesis now enable precise control over π-conjugation, molecular curvature, and heteroatom incorporation, leading to chiral systems that simultaneously exhibit high luminescence efficiency and large $|g_{lum}|$ values (Table 1). These properties underpin their growing use in circularly polarized light detection, bioimaging, information encryption, and 3D display technologies.

Despite this progress, key challenges remain. A major limitation is the lack of systematic and scalable synthetic strategies for producing structures with well-defined morphology, functional groups, defect sites, and doping profiles. Moreover, the use of non-standardized synthetic pathways and the presence of impurities obscure the underlying mechanisms of chiral induction and transfer. The origin of circularly polarized luminescence also remains contentious due to structural variability and diverse assembly strategies. Addressing these issues will require deeper theoretical insights and high-precision structural characterization to clarify CPL generation mechanisms. Moving forward, integrating computational modeling with automated synthesis platforms may accelerate the discovery and optimization of next-generation chiral carbon materials, enabling practical applications in areas such as circularly polarized OLEDs and beyond.

Conflicts of interest

There are no conflicts to declare.

Data availability

No primary research results, software or code have been included and no new data were generated or analyzed in this review.

Acknowledgements

L. W. acknowledges the financial support from the European Union (ERC Starting Grant, FastE-Chiral, no. 101162601). X. Z., X. G., J. Y., Y. W., and Q. H. acknowledge support from the Program for Jiangsu Specially-Appointed Professors and the Nantong Youth Science and Technology Talent Fund (JC2024032). Open Access funding provided by the Max Planck Society.

References

1 W. Q. Wang, *Acta Sci. Nat. Univ. Pekin.*, 1997, **33**, 265–272.
2 Q. S. Zhu, *Bull. Biol.*, 2015, **50**, 17–20.
3 Y. Zhao, J. Li and C. Zhan, *Sci. Sin. Chim.*, 2024, **54**, 1212–1232.
4 C. Du, Z. J. Li, X. F. Zhu, G. H. Ouyang and M. H. Liu, *Nat. Nanotechnol.*, 2022, **17**, 1294–1302.
5 X. B. Shang, L. Wan, L. Wang, F. Gao and H. Y. Li, *J. Mater. Chem. C*, 2022, **10**, 2400–2410.
6 J. J. Tong, Y. Cao, Y. W. Zhang, P. Wang, P. L. Wang, X. J. Liao, W. G. Zhang, Y. Wang, Y. X. Zheng, J. J. Zhu and Y. Pan, *Angew. Chem., Int. Ed.*, 2022, **61**, e202209438.
7 G. Wang, M. H. Yu and X. L. Feng, *Chem. Soc. Rev.*, 2021, **50**, 2388–2443.
8 F. Saal, V. Brancaccio, K. Radacki, H. Braunschweig and P. Ravat, *Angew. Chem., Int. Ed.*, 2025, e202508779, DOI: 10.1002/anie.202508779.
9 X. H. Niu, Y. Q. Liu, R. Zhao, L. H. Wang, M. Yuan, H. F. Zhao, H. X. Li, X. Yang and K. J. Wang, *J. Mater. Chem. A*, 2024, **12**, 17073–17127.
10 E. Benchimol, H. M. O'Connor, B. Schmidt, N. Bogo, J. J. Holstein, J. I. Lovitt, S. Shanmugaraju, C. J. Stein, T. Gunnlaugsson and G. H. Clever, *Angew. Chem., Int. Ed.*, 2025, **64**, e202421137.
11 L. Ai, H. L. Wang, B. Y. Wang, S. Y. Liu, H. Q. Song and S. Y. Lu, *Adv. Mater.*, 2024, **36**, 2410094.
12 Y. M. Wang, W. H. Zhang and Y. P. Zhai, *Univ. Chem.*, 2007, **22**, 52–57.
13 W. W. Zhang, Q. N. Wang, C. Zheng and S. L. You, *ACS Catal.*, 2025, **15**, 4017–4024.

14 M. Rickhaus, M. Mayor and M. Jurícek, *Chem. Soc. Rev.*, 2016, **45**, 1542–1556.
15 B. P. Bloom, Z. Chen, H. Lu and D. H. Waldeck, *Natl. Sci. Rev.*, 2024, **11**, nwae212.
16 G. Zhang, X. Cheng, Y. Wang and W. Zhang, *Aggregate*, 2023, **4**, e262.
17 K. Mao, C. Liu, Y. Wang, C. Gu, J. M. Putziger, N. I. Cemalovic, C. Muniz, Y. Qi and S. Lin, *Nature*, 2025, **643**, 1288–1296.
18 Y. Chen, J. Zhang, J. Zhang and X. Wan, *J. Am. Chem. Soc.*, 2024, **146**, 9679–9687.
19 G. K. Long, R. Sabatini, M. I. Saidaminov, G. Lakhwani, A. Rasmita, X. G. Liu, E. H. Sargent and W. B. Gao, *Nat. Rev. Mater.*, 2020, **5**, 423–439.
20 M. M. Moein and T. A. Tran, *J. Chromatogr. A*, 2020, **1632**, 461611.
21 J. M. Han, S. Guo, H. Lu, S. J. Liu, Q. Zhao and W. Huang, *Adv. Opt. Mater.*, 2018, **6**, 1800538.
22 J. H. Jiang, F. L. Ma, R. H. Dong, S. W. Zhang, Z. C. Zhang, H. Z. Tan, X. M. Cai, Z. J. Qiu, Y. Xiong, W. Han, Z. Zhao and B. Z. Tang, *J. Am. Chem. Soc.*, 2023, **145**, 27282–27294.
23 S. Z. Jia, B. B. Yang, Y. J. Xie, T. T. Tao, J. Du, L. Y. Yu, Y. Zhang, J. Y. Zhang, W. W. Tang and J. B. Gong, *Adv. Funct. Mater.*, 2024, **34**, 2410206.
24 H. Tanaka, Y. Inoue and T. Mori, *ChemPhotoChem*, 2018, **2**, 386–402.
25 L. Arrico, L. Di Bari and F. Zinna, *Chem. – Eur. J.*, 2021, **27**, 2920–2934.
26 J. L. Greenfield, J. Wade, J. R. Brandt, X. Y. Shi, T. J. Penfold and M. J. Fuchter, *Chem. Sci.*, 2021, **12**, 8589–8602.
27 M. J. Ji, W. L. Zhao, M. Li and C. F. Chen, *Nat. Commun.*, 2025, **16**, 2940.
28 X. F. Luo, H. B. Han, Z. P. Yan, Z. G. Wu, J. Su, J. W. Zou, Z. Q. Zhu, Y. X. Zheng and J. L. Zuo, *ACS Appl. Mater. Interfaces*, 2020, **12**, 23172–23180.
29 T. Mori, *Circularly polarized luminescence of isolated small organic molecules*, Springer, 2020.
30 L. Gao, R. Liao, L. Ao, Y. Zhang, J. Jin and F. Wang, *Angew. Chem., Int. Ed.*, 2025, **64**, e202505776.
31 C. H. Guo, W. L. Zhao, K. K. Tan, W. C. Guo, L. H. Feng, C. F. Chen and M. Li, *Sci. China: Chem.*, 2024, **67**, 2039–2045.
32 M. Li, Y. F. Wang, D. Zhang, L. Duan and C. F. Chen, *Angew. Chem., Int. Ed.*, 2020, **59**, 3500–3504.
33 Z. L. Tu, J. J. Lu, X. F. Luo, J. J. Hu, S. Li, Y. Wang, Y. X. Zheng, J. L. Zuo and Y. Pan, *Adv. Opt. Mater.*, 2021, **9**, 2100596.
34 Z. P. Yan, T. T. Liu, R. X. Wu, X. Liang, Z. Q. Li, L. Zhou, Y. X. Zheng and J. L. Zuo, *Adv. Funct. Mater.*, 2021, **31**, 2103875.
35 J. F. Chen, Q. X. Gao, H. Yao, B. B. Shi, Y. M. Zhang, T. B. Wei and Q. Lin, *Chem. Commun.*, 2024, **60**, 6728–6740.
36 Y. Morisaki, M. Gon, T. Sasamori, N. Tokitoh and Y. Chujo, *J. Am. Chem. Soc.*, 2014, **136**, 3350–3353.
37 J. F. Chen, Q. X. Gao, L. J. Liu, P. K. Chen and T. B. Wei, *Chem. Sci.*, 2023, **14**, 987–993.
38 X. T. Liang, Y. L. Shen, D. Y. Zhou, J. C. Ji, H. T. Wang, T. Zhao, T. Mori, W. H. Wu and C. Yang, *Chem. Commun.*, 2022, **58**, 13584–13587.
39 X. N. Han, Y. Han and C. F. Chen, *J. Am. Chem. Soc.*, 2020, **142**, 8262–8269.
40 M. H. Gong, L. Yuan, Y. X. Zheng and W. H. Zheng, *Adv. Funct. Mater.*, 2024, **34**, 2314205.
41 Z. Y. Jiang, Z. Chen, X. J. Yu, S. Lu, W. M. Xu, B. Yu, C. L. Stern, S. Y. Li, Y. Zhao, X. Z. Liu, Y. Q. Han, S. Q. Chen, K. Cai, D. K. Shen, K. K. Ma, X. P. Li and A. X. Y. Chen, *J. Am. Chem. Soc.*, 2025, **147**, 7325–7335.
42 A. Nowak-Król, P. T. Geppert and K. R. Naveen, *Chem. Sci.*, 2024, **15**, 7408–7440.
43 Y. Qiu, X. L. Wei, J. W. Y. Lam, Z. J. Qiu and B. Z. Tang, *ACS Nano*, 2025, **19**, 229–280.
44 C. M. Shi, H. L. Lu, J. Y. Wang, G. K. Long, L. J. Xu and Z. N. Chen, *Nat. Commun.*, 2025, **16**, 1505.
45 M. S. Newman and D. Lednicer, *J. Am. Chem. Soc.*, 1956, **78**, 4765–4770.
46 K. Mori, T. Murase and M. Fujita, *Angew. Chem., Int. Ed.*, 2015, **54**, 6847–6851.
47 Z. J. Qiu, C. W. Ju, L. Frédéric, Y. B. Hu, D. Schollmeyer, G. Pieters, K. Müllen and A. Narita, *J. Am. Chem. Soc.*, 2021, **143**, 4661–4667.
48 C. M. Cruz, S. Castro-Fernández, E. Maçôas, J. M. Cuerva and A. G. Campaña, *Angew. Chem., Int. Ed.*, 2018, **57**, 14782–14786.
49 S. Míguez-Lago, I. F. A. Mariz, M. A. Medel, J. M. Cuerva, E. Maçôas, C. M. Cruz and A. G. Campaña, *Chem. Sci.*, 2022, **13**, 10267–10272.
50 Y. J. Shen, N. T. Yao, L. N. Diao, Y. Yang, X. L. Chen and H. Y. Gong, *Angew. Chem., Int. Ed.*, 2023, **62**, e202300840.
51 N. Wei, Y. R. Ding, J. Q. Zhang, L. Y. Li, M. Q. Zeng and L. Fu, *Nat. Sci. Rev.*, 2023, **10**, nwad145.
52 M. Srsen, S. K. Pedersen, T. Rozic, A. Lanza and M. Pittelkow, *Angew. Chem., Int. Ed.*, 2025, **64**, e202506328.
53 Y. Han, S. Wu, K. Y. S. Khoo and C. Chi, *Nat. Synth.*, 2025, **4**, 947–955.
54 Z. J. Qiu, S. Asako, Y. B. Hu, C. W. Ju, T. Liu, L. Rondin, D. Schollmeyer, J. S. Lauret, K. Müllen and A. Narita, *J. Am. Chem. Soc.*, 2020, **142**, 14814–14819.
55 M. A. Medel, R. Tapia, V. Blanco, D. Miguel, S. P. Morcillo and A. G. Campaña, *Angew. Chem., Int. Ed.*, 2021, **60**, 6094–6100.
56 M. A. Medel, C. M. Cruz, D. Miguel, V. Blanco, S. P. Morcillo and A. G. Campaa, *Angew. Chem., Int. Ed.*, 2021, **60**, 22051–22056.
57 L. Yang, Y. Y. Ju, M. A. Medel, Y. B. Fu, H. Komber, E. Dmitrieva, J. J. Zhang, S. Obermann, A. G. Campana, J. Ma and X. L. Feng, *Angew. Chem., Int. Ed.*, 2023, **62**, e202216193.
58 I. Boudjahem, A. Nemamcha, H. Moumeni and N. Brahimi, *Struct. Chem.*, 2024, **36**, 947–974.
59 D. Reger, P. Haines, F. W. Heinemann, D. M. Guldi and N. Jux, *Angew. Chem., Int. Ed.*, 2018, **57**, 5938–5942.
60 P. An, R. R. Li, B. Ma, R. Y. He, Y. K. Zhang, M. J. Xiao and B. Zhang, *Angew. Chem., Int. Ed.*, 2021, **60**, 24478–24483.
61 H. Zhou, Y. F. Ao, D. X. Wang and Q. Q. Wang, *J. Am. Chem. Soc.*, 2022, **144**, 16767–16772.

62 Y. Y. Zhou, H. F. Li, T. Y. Zhu, T. Gao and P. F. Yan, *J. Am. Chem. Soc.*, 2019, **141**, 19634–19643.
63 Y. L. Sun, Z. Wang, H. Ma, Q. P. Zhang, B. B. Yang, X. G. Meng, Y. H. Zhang and C. Zhang, *Chem. Commun.*, 2023, **59**, 302–305.
64 R. Chowdhury, M. D. Preuss, H. H. Cho, J. J. P. Thompson, S. Sen, T. K. Baikie, P. Ghosh, Y. Boeije, X. W. Chua, K. W. Chang, E. R. Guo, J. van der Tol, B. W. L. van den Bersselaar, A. Taddeucci, N. Daub, D. M. Dekker, S. T. Keene, G. Vantomme, B. Ehrler, S. C. J. Meskers, A. K. Rao, B. Monserrat, E. W. Meijer and R. H. Friend, *Science*, 2025, **387**, 1175–1181.
65 C. Q. Li, H. Wu, T. K. Zhang, Y. J. Liang, B. Zheng, J. Xia, J. B. Xu and Q. Miao, *Chem*, 2018, **4**, 1416–1426.
66 F. L. Qiu, X. T. Zhang, W. J. Wang, K. Z. Su and D. Q. Yuan, *J. Am. Chem. Soc.*, 2025, **147**, 8500–8512.
67 S. M. Jing, Z. G. Gu and J. Zhang, *J. Am. Chem. Soc.*, 2025, **147**, 8948–8958.
68 H. Chen, Z. G. Gu and J. Zhang, *J. Am. Chem. Soc.*, 2022, **144**, 7245–7252.
69 B. Zhou, L. H. Cao, M. F. Huang, Y. Yang, S. M. Qi, X. J. Cao and X. Y. Chen, *Angew. Chem., Int. Ed.*, 2025, **64**, e202504645.

